Analysis of gravity-driven infiltration with the development of a saturated region

Mohammad Afzal Shadab[1,2] **and Marc Andre Hesse**[1,3]

[1]Oden Institute for Computational Engineering and Sciences, The University of Texas at Austin, 201 E. 24th Street, C0200, Austin, TX 78712, USA
[2]University of Texas Institute for Geophysics, The University of Texas at Austin, 10601 Exploration Way, Austin, TX 78758
[3]Department of Geological Studies, Jackson School of Geosciences, The University of Texas at Austin, 2305 Speedway, C1160, Austin, TX 78712, USA

Key Points:

- Formulated an extended kinematic wave analysis for one-dimensional infiltration with coupled unsaturated and saturated regions.
- Transitional infiltration into soil with decaying conductivity leads to the formation of a saturated region and rising perched water table.
- Semi-analytic solutions with formation and evolution of a saturated region provide challenging benchmarks for numerical solutions (Hydrus).

Corresponding author: Mohammad Afzal Shadab, mashadab@utexas.edu

This article has been accepted for publication and undergone full peer review but has not been through the copyediting, typesetting, pagination and proofreading process, which may lead to differences between this version and the Version of Record. Please cite this article as doi: 10.1029/2022WR032963.

Abstract

Understanding the controls on the infiltration of precipitation into soil is an important problem in hydrology and its representation in heterogeneous media is still challenging. Here we investigate the reduction of gravity-driven infiltration by the development of a saturated region due to the downward decrease in porosity and/or hydraulic conductivity. The formation of a saturated region chokes the flow and leads to a rising perched water table that causes ponding even when rainfall intensity is lower than the surface infiltration capacity. Mathematically this problem is interesting, because its governing partial differential equation switches from hyperbolic in the unsaturated region to elliptic in the saturated region. To analyze this coupled unsaturated-saturated flow we develop an extended kinematic wave analysis in the limit of no capillary forces. This theory provides a general framework to solve gravity-dominated infiltration problems for arbitrary downward decrease in porosity and/or conductivity. We apply the framework to three soil profiles (two-layer, exponential and power-law decay with depth) and develop (semi-) analytic solutions for evolution of the water saturation. For the case of a two-layer soil the saturated flux, and therefore the front speeds, are constant which allows explicit analytic solutions that agree well with Hydrus-1D. All solutions show excellent agreement with our numerical solutions of the governing equations in the limit of no capillary forces. Similarly, our solutions compare well with experimental data for infiltration into a multi-layer soil with declining hydraulic conductivity.

Plain Language Summary

Understanding the rainfall into a heterogeneous medium is crucial to estimate the time when rainwater will pond on the surface and begin to form runoff. Previous work has focused on the limiting cases: limited rainfall where the soil is always unsaturated and water never ponds on the surface and excessive rainfall where the soil is always saturated but ponding is initially prevented by capillary suction. Here we focus on the case of transitional rainfall where soil dynamically switches from unsaturated to saturated if hydraulic conductivity declines with depth. In this case, all rainwater initially infiltrates until a perched water table forms in the soil. If rainfall is sustained long enough this perched water table rises to the surface and water begins to pond and runoff is generated. The dynamics can be compared to filling a leaking bucket, where rise of the water level in the bucket depends on the rate of leakage through the base. The motion of such water fronts is studied by extending an established mathematical theory, which ultimately yields simple analytical solutions.

Symbols and notations

Symbol	Definition (SI Units)
R	Rainfall intensity (m/s)
K_s	Saturated hydraulic conductivity at surface (m/s)
f_c	Surface infiltration capacity (m/s)
K_m	Minimum sat. hydraulic conductivity across soil profile (m/s)
ϕ	Porosity (or volume fraction in Figures 3, 8 and 10) (m^3/m^3)
k	Intrinsic or absolute permeability of the soil (m^2)
s	Water saturation (m^3/m^3)
t	Time variable (s)
z	Depth coordinate (m)
$K(s)$	Saturation dependent hydraulic conductivity (m/s)
Ψ	Capillary suction head or matric head (m)
k_{rw}	Relative permeability of water phase (-)
ρ	Density of water phase (kg/m^3)

g	Acceleration due to gravity (m/s^2)
μ	Dynamic viscosity of water (Pa.s)
s_{wr}	Residual water phase saturation (m^3/m^3)
s_{gr}	Residual gas phase saturation (m^3/m^3)
Pe	Peclet number:= Advective transport / diffusive transport (-)
θ	Soil moisture content = Saturation×Porosity (m^3/m^3)
D	Soil water diffusivity (m^2/s)
h	Hydraulic head (m)
Ω_s	Domain of complete saturation
p	Pressure of water phase (Pa)
$\partial\Omega_s$	Interface between saturated and unsaturated domains
v	Velocity of the interface (m/s)
q	Flux of water phase (m/s)
q_u	Unsaturated flux across the interface (m/s)
q_s	Saturated flux across the interface (m/s)
s_u	Saturation on the unsaturated side of the interface (m^3/m^3)
s_s	Saturation on the fully-saturated side of the interface (m^3/m^3)
$\overline{K}$	Harmonic mean of hydraulic conductivity (m/s)
z_k	Location or depth of the shock front k (m)
t_s	Time of formation of saturated region (s)
t_p	Time of ponding (s)
$\mathcal{S}_k$	Speed of the shock front k (m/s)
ϵ	Infinitesimally small depth, $0 < \epsilon \ll 1$ (m)
z_s	Location or depth where saturated region forms (m)
t_u	Time upper shock takes to reach the surface since its formation (s)
m	Porosity-permeability power law model constant (-)
n	Relative permeability-effective saturation power law model constant (-)
k_0	Absolute permeability at unity porosity, a model constant (m^2)
K_0	Saturated hydraulic conductivity at unity porosity, a model constant (m/s)
s_e	Effective water saturation (-)
z_0	Characteristic depth (or location of the porosity jump in two-layered soil) (m)
l	Thickness of the saturated region (m)
$\mathfrak{C}$	Ratio of upper shock speed to lower shock speed (-)
u_p	Pore or interstitial velocity of the water phase (m/s)
p	Power-law porosity decay exponent (-)
K_o	Saturated hydraulic conductivity at the surface (m/s)
f	Conductivity decay coefficient (m^{-1})
Ψ_{wf}	Green and Ampt wetting front potential (m)
$\Delta\theta$	Available pore space (m^3/m^3)
I_c	Cumulative infiltration (m)
C	Storage suction factor (m)
$\mathbf{q}$	Volumetric flux vector of water phase (m/s)
k_{rg}	Relative permeability of the gas phase (-)
$\mathbf{g}$	Acceleration due to gravity vector (m/s^2)
p_c	Capillary pressure:= Difference between gas and water pressures (Pa)
q_T	Total flux of water across the domain (m/s)
$\mathcal{F}$	Advective flux of the water phase (m/s)
$\mathcal{D}$	Diffusive flux of the water phase (m/s)

Subscripts

$\partial\Omega_s$	Variable evaluated at the interface $\partial\Omega_s$
f	Variable corresponding to the initial wetting front
u	Variable corresponding to the upper shock (or upper layer in two-layer soil)
l	Variable corresponding to the lower shock (or lower layer in two-layer soil)
i	Initial value of variable inside the soil at a specific location
$+$	Variable evaluated on the lower side of shock
$-$	Variable evaluated on the upper side of shock
0	Characteristic variable or variable evaluated at the surface
g	Variables corresponding to gas phase instead of water phase

Superscripts

$'$	Dimensionless equivalent of the corresponding variable
0	Variable evaluated at complete saturation (end-point)

1 Introduction

Infiltration is the entry of surface water into soil and its subsequent downward migration (Brutsaert et al., 2005). It partitions surface water into runoff and subsurface water and is therefore a crucial element of the hydrological cycle (Morbidelli et al., 2018a). Infiltration affects a myriad of processes both natural and anthropogenic, e.g., groundwater recharge, irrigation, flooding, and erosion (see Vereecken et al. (2019) for review). Infiltration of rain or surface water is a complex process that depends on many factors such as soil type, vegetation, topography, rainfall conditions and anthropogenic factors (Te Chow, 2010; Morbidelli et al., 2018a). While the quantitative study of infiltration has a long history, see Assouline (2013) for a historical review, the subject has received renewed interest due to its essential role in Land Surface Models (LSMs) (Clark et al., 2015). These LSMs are an important components of larger-scale Earth System Models (ESMs) needed to understand changes in the hydrologic cycle due to climate change and to develop societal adaptation strategies.

As such, infiltration has been the subject of several recent reviews by Morbidelli et al. (2018b), Vereecken et al. (2019) and Nimmo (2021) that highlight the need for continued improvements of our understanding of the physical processes, their incorporation into infiltration models and their representation in LSMs and ESMs. Among the challenges they identify are the heterogeneity of the soil physical properties and their upscaling, macro-porosity, front instability and preferential flow. In this study, we address some of the challenges posed by vertical soil heterogeneity (Keller & Or, 2022). Changes in soil properties with depth control the infiltration of water and hence the time until ponding and the formation of runoff (Vereecken et al., 2019). In particular, the presence of low conductivity horizons or decreases of conductivity with depth restrict infiltration (Kale & Sahoo, 2011) and may lead to the formation of a rising perched water table that is essential for runoff estimation in LSMs (Dai et al., 2019).

Infiltration is commonly characterized in terms of the rainfall intensity, R (m/s), the saturated hydraulic conductivity at the surface, K_s (m/s) and the infiltration capacity, f_c (m/s). The infiltration capacity of a partially saturated soil can exceed its saturated hydraulic conductivity temporarily due to capillary suction, $K_s \leq f_c$ (Horton, 1933). Based on these quantities Mein and Larson (1973) differentiate the following three infiltration cases:

(a) Rainfall limited infiltration, $R < K_s$: All rainwater infiltrates the soil so that ponding and runoff do not occur.
(b) Transitional infiltration, $K_s < R \leq f_c$: All rainwater initially infiltrates due to capillary suction. Only as capillary suction declines water begins to pond and therefore runoff is delayed.
(c) Percolation limited infiltration, $K_s < f_c \leq R$: The rainfall exceeds the infiltration capacity, so that water ponds instantaneously and runoff occurs immediately.

The transitional infiltration (b) is the most challenging for models, because they need to capture the delay in ponding and runoff generation. In a dry homogeneous soil transitional behavior occurs because the infiltration capacity declines with time, due to reduction in capillary suction as the wetting front spreads out (Philip, 1957). The runoff generated from this process is commonly referred to as Hortonian overland flow (Horton, 1933). However, ponding in homogeneous soils can also occur during the rainfall limited infiltration (a) if the water table is shallow so that continued infiltration fills up the available pore space. Runoff generated by this mechanism is commonly referred to as Dunne overland flow (Dunne, 1978).

In heterogeneous soils ponding can also occur in absence of both capillary forces and a shallow water table. A decline of hydraulic conductivity with depth or the presence of a low conductivity layer at depth can lead to the formation of a saturated layer that restricts infiltration and leads to the formation of a rising perched water table. Once the perched water table reaches the surface ponding begins and the runoff is generated. However, in contrast to Dunne overland flow where infiltration ceases, in this case infiltration may continue after ponding. This behavior occurs if $K_m < R \leq f_c$, where K_m is the minimum hydraulic conductivity of the soil profile, $0 < K_m < K_s$.

For the purpose of this study we refer to this behavior in heterogeneous soils as transitional, because infiltration transitions from rainfall limited to percolation limited. Here we investigate the dynamics of transitional infiltration due to vertical soil heterogeneity and develop (semi-) analytic solutions for the saturation evolution. For simplicity we assume constant rainfall, R, and gravity dominated infiltration, i.e., negligible capillary forces ($f_c = K_s$). Below we briefly summarize relevant previous work, but point to recent reviews mentioned above for more extensive summaries.

Infiltration is typically modeled with Richards equation which describes the water movement due to gravity and capillary forces in a partially saturated soil (Richards, 1931; Philip, 1957). It remains the standard for infiltration modeling, in particular in LSMs (Vereecken et al., 2019), although it fails to describe commonly observed phenomena such as the instability of the wetting front, saturation overshoots and the formation of preferential flow path (DiCarlo, 2013; Nimmo, 2021). While some of these features can be described with extensions of Richards equation (Hassanizadeh & Gray, 1993; DiCarlo, 2005; Cueto-Felgueroso & Juanes, 2008), most work on infiltration instead relies on the simplifications of Richards equation.

The most commonly used infiltration model was developed by Green and Ampt (1911) which assumes a sharp wetting front resulting in a saturated medium behind the wetting front, and including the effect of capillary suction. This allows it to represent transitional infiltration due to capillary suction (Mein & Larson, 1973). Over time this model has been extended and modified numerous times to account for heterogeneous soils and complex rainfall patterns, see Kale and Sahoo (2011) for a review. Most relevant to the work presented here are the studies extending the Green-Ampt approach to layered soils (Childs & Bybordi, 1969; Mein & Larson, 1973; Corradini et al., 2000) and to exponentially decaying conductivity profiles (Beven, 1984; Selker et al., 1999). However, none of these studies consider the formation and growth of a perched water table at a later stage due to soil heterogeneity.

Another simplification of Richards equation is the kinematic wave approximation (Sisson et al., 1980; Smith, 1983; Charbeneau, 1984). It neglects capillary forces but captures the dynamics of gravity-driven unsaturated flow and has been used to study water infiltration, redistribution and drainage in soil and snow (Colbeck, 1972; Singh et al., 1997; Clark et al., 2017; Meyer & Hewitt, 2017). This approximation leads to a non-linear wave equation that allows solution by the Method Of Characteristics (MOC). Analysis with the MOC identifies the types of waves (fronts) and their interactions (Rhee et al., 2001; LeVeque, 1992), which provides fundamental insights into the dynamics of infiltration. A limitation of the kinematic wave approximation is that it only applies to unsaturated flow. Below we show that, for one- dimensional cases, this theory can be extended to include flow in the saturated zone. As such it the best tool to study gravity driven infiltration in the limit of negligible capillarity with formation of saturated zones due to vertical heterogeneity in the soil profile.

In this paper, we investigate the case of transitional infiltration into soils with vertical heterogeneity. The initial wetting front does not saturate the soil but the flow chokes later due to formation of a saturated region at depth and forms a rising perched water table. In section 2, we introduce Richards equation and the kinematic wave approximation for gravity-dominated unsaturated flow. Further, the fully-saturated region is integrated into the analysis of unsaturated flow by introducing the extended kinematic wave approximation. In section 3, the tools from hyperbolic analysis are used to investigate the physics of infiltration in a dry heterogeneous soil due to transitional infiltration. A general framework is developed to solve the gravity-dominated infiltration problem for transitional infiltration, along with ponding time estimates for general hydraulic conductivity and porosity decay with depth. Section 4 develops (semi-) analytic solutions for three specific soil profiles with step-reduction (two-layered), exponential and power law decay with depth. The two-layered soil is studied using tools from the theory of hyperbolic conservation laws to understand the water parcel and wave motions after entering the soil. In Section 5 we compare our analytical solution for the two-layered soil to full solutions of Richards equation using Hydrus 1D and apply our theory to the experimental data of Childs and Bybordi (1969) to explore the effect of neglecting capillary suction.

2 Governing equations for gravity-dominated infiltration

2.1 Gravity-dominated limit of Richards equation and its physics based extension to fully-saturated regions

The system is composed of two fluid phases, water and gas, in a non-deforming and stationary porous medium with porosity ϕ and permeability k. For rainwater infiltration into soil both density and viscosity of gas are much smaller than that of water. In this limit, the gas responds essentially instantaneously and its pressure can be assumed a constant, so that only the flow of water is considered. Therefore the full two-phase flow equations corresponding to gas and water phases reduce to a single Richards equation (Richards, 1931; Richardson, 1922) also known as Richardson-Richards equation (Zha et al., 2019). In one-dimension the saturation form of Richards equation is given by

$$\phi \frac{\partial s}{\partial t} + \frac{\partial}{\partial z}\left[K(s)\left(\frac{\partial \Psi(s)}{\partial z} + 1\right)\right] = 0, \tag{1}$$

where s is the water saturation, z is the depth coordinate (m), t is the time variable (s). Moreover, $K(s) = \mathrm{k} k_{rw}(s)\rho g/\mu$ is the saturation-dependent hydraulic conductivity (m/s) with g being the acceleration due to gravity (m/s^2), ρ being the density (kg/m^3) and μ being the dynamic viscosity (Pa s) of the water phase. Relative permeability of water, k_{rw}, is a function of water saturation, s (Wyckoff & Botset, 1936). The absolute permeability of the porous medium, given by k (m^2), is a function of the porosity ϕ. The

capillary suction head, Ψ (m), relates the two fluid pressure heads and is typically assumed to be a function of saturation only (Leverett, 1941; Brooks & Corey, 1964; van Genuchten, 1980). The constitutive functions for multi-phase flow, k_{rw} and Ψ, display complex hysteresis (Blunt, 2017), but here we only consider the simplest case. We assume that water phase becomes immobile below a certain residual water saturation, s_{wr}, and similarly the gas phase becomes immobile below the residual gas saturation, s_{gr}. As a result, the two-phase flow is restricted to regions where $s_{wr} < s < 1 - s_{gr}$. Below we will refer to regions with $s = 1 - s_{gr}$ as saturated, although immobile gas bubbles are still present (Figure 1). The standard relations for the capillary pressure (Brooks & Corey, 1964) introduce singularities in the limit of fully saturated porous media, which are commonly removed heuristically (Clapp & Hornberger, 1978) to reduce numerical problems (Farthing & Ogden, 2017).

Richards equation (1) can be derived from the full two-phase flow formulation (A1-A5) as given in Appendix B. Here we further assume the problem is gravity dominated such that the spatial change in suction head is negligible at the problem length scales, i.e., $\partial\Psi/\partial z \ll 1$. This limit occurs when the ratio of advective transport to diffusive transport, known as Peclet number (Pe) is very high. Smith (1983) showed that the appropriate definition for Richards equation is

$$Pe = \frac{K(\theta)}{D(\theta)\partial\theta/\partial z}, \tag{2}$$

where $\theta = \phi s$ is the soil moisture content and soil water diffusivity is given by $D(\theta) = K(\theta)\mathrm{d}\Psi/\mathrm{d}\theta$ (m^2/s). The limit of high Pe occurs in low-textured soils such as sand where capillary forces are weak or when the length scale considered is large. In this limit, Richards equation (1) simplifies to the following hyperbolic form in an unsaturated medium

$$\phi\frac{\partial s}{\partial t} + \frac{\partial K(s)}{\partial z} = 0. \tag{3}$$

This limit is commonly referred to as the kinematic wave approximation (Smith, 1983; Charbeneau, 1984; Milly, 1988). This equation is naturally one-dimensional, if gravity is aligned with a coordinate direction. Even in a multi-dimensional, heterogeneous and isotropic medium any unsaturated front, modeled using hyperbolic form of Richards equation (3), will migrate strictly in the vertical direction. This changes only when the medium saturates locally and pressure gradients couple the flow in all directions across the saturated region. In a saturated region, Equations (A3) and (A4) limit to the elliptic equation for incompressible saturated flow

$$-\nabla\cdot(K\nabla h) = 0 \quad \text{in} \quad \Omega_s(t), \tag{4}$$

where $h = p/(\rho g) - z$ is the hydraulic head (m) with p being the pressure of the water phase (Pa). We have used K to refer to the saturated hydraulic conductivity, which is strictly $K(1-s_{gr})$. To solve problems of infiltration in the gravity-dominant limit requires the dynamic coupling between the hyperbolic (3) and elliptic regions (4). Although (4) itself is not time dependent the saturated domain, $\Omega_s(t)$, changes with time due to its interaction with the unsaturated region.

We refer to the interface between the saturated and unsaturated regions simply as the interface and denote it as $\partial\Omega_s$ (Figure 1). The water pressure in the unsaturated region is determined by the gas and hence set to zero because both capillary and gas pressures are assumed to be negligible (see Appendix B). Therefore, the hydraulic head boundary condition along the interface is simply,

$$h = -z \quad \text{at} \quad z \in \partial\Omega_s. \tag{5}$$

The velocity of the interface $v_{\partial\Omega_s}$, is determined by discrete mass balance across the interface via spatially integrating equation (7) around the interface as

$$v_{\partial\Omega_s} = \frac{(q_u - q_s)}{\phi_u s_u - \phi_s(1 - s_{gr})}, \tag{6}$$

where q_u and q_s are the unsaturated and saturated fluxes along the interface and $\phi_u s_u = \theta_u$ and $\phi_s(1-s_{gr}) = \theta_s$ are the soil moisture contents (water volume fractions) on the unsaturated and saturated sides of the interface. The boundary of the saturated domain, $\partial\Omega_s$, evolves according to this interface velocity.

2.2 Extended kinematic wave approximation for gravity-dominated infiltration with formation of a saturated region in one dimension

Here we develop analytic and semi-analytic solutions to this coupled system of hyperbolic and elliptic equations (3-4) in one dimension (1D), to study the effect of decreasing porosity with depth on transitional infiltration (Figure 1). We denote the upper and lower boundaries of the saturated region, $\partial\Omega_s$, as z_u and z_l, respectively. The problem simplifies in 1D, because (4) can be integrated to obtain the saturated flux explicitly. This allows us to write the problem solely in terms of the hyperbolic equation for the saturation

$$\phi \frac{\partial s}{\partial t} + \frac{\partial q(s,t)}{\partial z} = 0, \tag{7}$$

with a piece-wise defined flux function

$$q(s,t) = \begin{cases} q_u = K(s), & s_{wr} \le s < 1 - s_{gr} \\ q_s = \overline{K}(t), & s = 1 - s_{gr} \end{cases} \tag{8}$$

for unsaturated and saturated regions respectively, where $\overline{K}$ is the harmonic mean of the hydraulic conductivity

$$\overline{K}(t) = \frac{z_l(t) - z_u(t)}{\int_{z_u(t)}^{z_l(t)} \frac{1}{K(z)} dz}, \tag{9}$$

over the saturated region, $\Omega_s(t) \in [z_u(t),\, z_l(t)]$. We emphasize that the saturated flux is time dependent, because the saturated region changes dynamically. In this formulation, the coupled hyperbolic-elliptic problem is converted into a hyperbolic system with a piece-wise defined flux that is not only a function of the dependent variable, s, but also a function of independent variable, t. We refer to this formulation as the *extended kinematic wave* formulation. The advantage of this formulation is that the motion of the interface (6) which describes the coupling between hyperbolic and elliptic regions is captured by the flux function. As such, it can be treated with standard tools from the analysis of hyperbolic conservation laws (Rhee et al., 2001; LeVeque, 1992). We are not aware of any other comparable system that is discussed in the literature.

In this manuscript we only consider problems with the formation of a single saturated region, but (7-9) are valid for any number of saturated regions. The analysis presented below can be extended to 1D cases with multiple saturated regions that interact.

3 Transitional infiltration with formation of a saturated region

Here we consider a semi-infinite one-dimensional domain where porosity and therefore the associated permeability decreases with increasing depth (Figure 1*b*). We assume

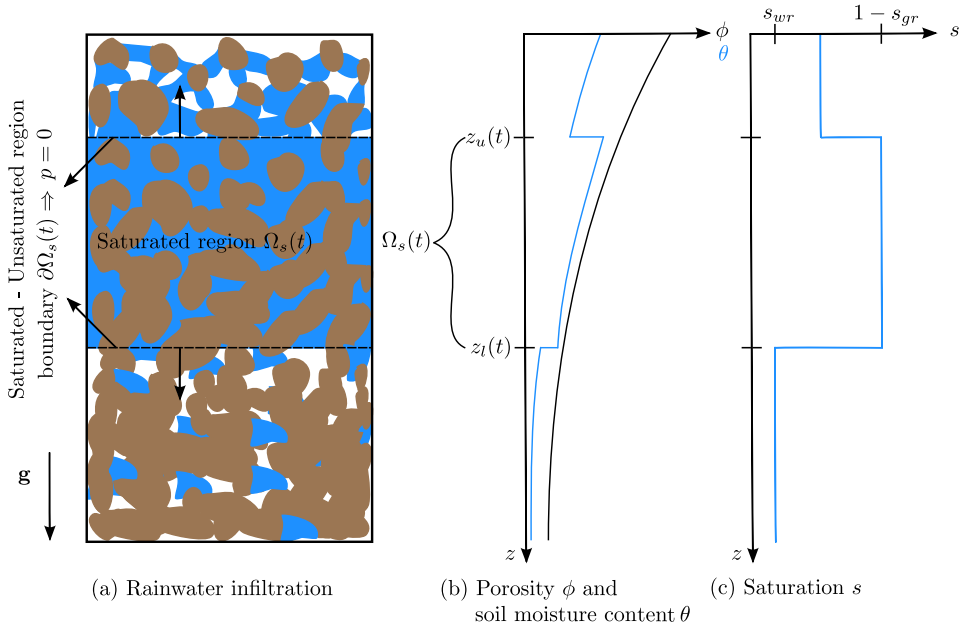

(a) Rainwater infiltration (b) Porosity ϕ and soil moisture content θ (c) Saturation s

Figure 1: Gravity-driven infiltration in an unsaturated soil with porosity ϕ decay with depth leading to formation a saturated region. (a) Schematic showing water, soil and gas phases with blue, brown, white colors respectively. (b) Porosity decay with depth, z. Moreover, soil moisture content, θ, variation and (c) water saturation, s, variation with depth at some time t when a fully saturated region, $\Omega_s(t)$, develops within the otherwise unsaturated domain.

that the soil is initially at residual water saturation and that rainfall intensity is less than the surface infiltration capacity. This case is interesting because a saturated region forms dynamically within the soil and controls the infiltration. The infiltration dynamics can be divided into three stages (Figure 2), on the basis of the time of formation of saturated region, t_s, and the time of water ponding on the surface, t_p.

1. Stage 1 ($t < t_s$): The flow is unsaturated, a wetting front propagates downwards and all rainfall infiltrates.
2. Stage 2 ($t_s \leq t < t_p$): Flow near the surface is still unsaturated and all rainfall continues to infiltrate. But a saturated region has formed at depth that chokes the flow and leads to a rising perched water table.
3. Stage 3 ($t \geq t_p$): The water table has risen to the surface where it causes ponding. All flow is now saturated and infiltration declines as the wetting front propagates into ever lower porosity soil.

Soils with declining porosity and transitional infiltration share these three stages. The solution is characterized by the motions of the wetting front and the perched groundwater table.

Analysis of the kinematic wave approximation enables the determination of the character and speed of these fronts. Charbeneau (1984) showed that fronts with a saturation increase are shocks, i.e. self-sharpening fronts with a discontinuity in saturation (Figure 1c). There exists a well-defined relation between the speed of a shock front and the jump of moisture content and flux across these waves (Navas-Montilla & Murillo, 2017). For the problem considered in this work, this relation comes only from the discrete mass balance across the shock wave by spatially integrating equation (7) in the vicinity of the

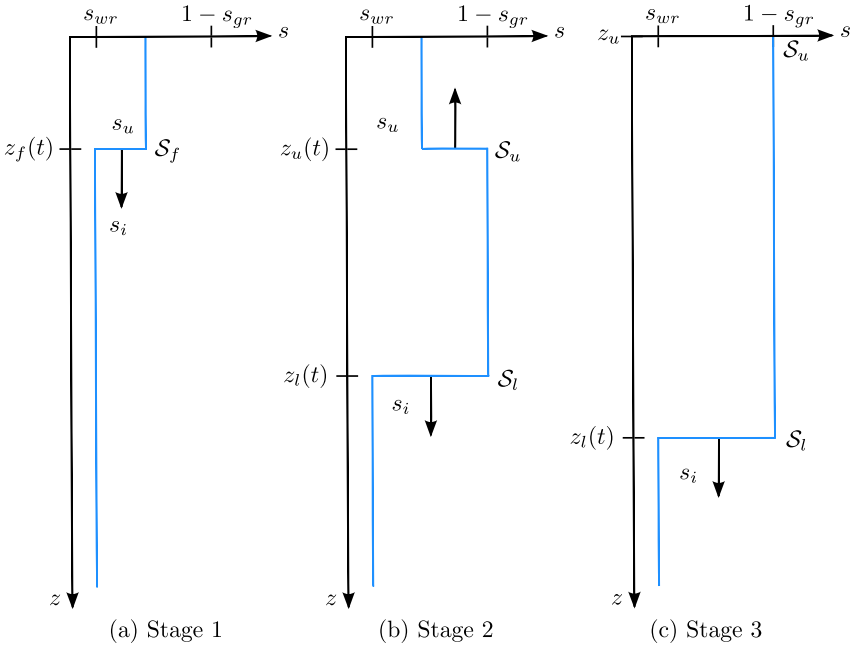

(a) Stage 1 (b) Stage 2 (c) Stage 3

Figure 2: Different stages of gravity-driven infiltration in an unsaturated soil with porosity ϕ decay with depth leading to formation a saturated region. (a) Stage 1 ($t < t_s$): Unsaturated gravity-driven infiltration. (b) Stage 2 ($t_s \le t < t_p$): Choking and formation of a rising perched water table. (c) Stage 3 ($t \ge t_p$): Saturated gravity-driven infiltration.

shock front, similar to derivation of (6). This relation is called Rankine-Hugoniot (RH) jump condition (LeVeque, 1992) which provides the shock speed

$$\mathcal{S}_k = \frac{\mathrm{d}z_k}{\mathrm{d}t} = \frac{[q(s,\phi)]}{[\phi\, s]} = \frac{q(s_+) - q(s_-)}{(\phi_+ s_+ - \phi_- s_-)} \tag{10}$$

where $\mathcal{S}_k$ and z_k are the speed (m/s) and location of the front. The subscript $k \in \{f,\, u,\, l\}$ can refer to any of the three shocks discussed below and shown in Figure 2. Here $[\,.\,]$ refers to the jump condition across the shock and subscripts $+$ and $-$ refer to the conditions on lower $(z_k + \epsilon)$ and upper $(z_k - \epsilon)$ sides of the shock front, where $\epsilon \ll 1$.

Previous work has applied the kinematic wave approximation only to unsaturated cases. Here we show that extended kinematic wave approximation (Section 2.2) also allows the analysis of saturated region. This is due to the explicit expression for the saturated flux in 1D. In this case, the motion of the interface, $\partial\Omega_s$, between the saturated and unsaturated regions, given by (6), reduces to the jump condition, $v_{\partial\Omega_s} = \mathcal{S}_{\partial\Omega_s}$. This allows the analysis of the dynamic interaction between saturated and unsaturated regions in the kinematic framework.

Below we first we develop a general theory for arbitrarily declining porosity profiles, before considering several special cases in Section 4. This is possible because although the particular front speeds and timings change, the three stages and the nature of the fronts are always the same.

3.1 Stage 1 ($t < t_s$): Unsaturated gravity-driven infiltration

At the beginning, the flow is unsaturated and the wetting front propagates downwards (Figure 2*a*), because the rainfall, R, is less than the infiltration capacity, $f_c = K_s$, during transitional infiltration. This stage is similar to the case (a) of limited rain-

fall ($R < K_s$) discussed in Section 1 where a fully saturated region does not form. Quantities related to this initial wetting front are denoted with subscript f. The speed of initial shock $\mathcal{S}_f$ can then be evaluated from (10) as

$$\mathcal{S}_f = \frac{\mathrm{d}z_f}{\mathrm{d}t} = \frac{R - q(s_i)}{\phi_u(s_u - s_i)} = \frac{R}{\phi_u(s_u - s_{wr})} \tag{11}$$

where s_u is the saturation above the wetting front and s_i is the initial saturation of the soil right below the front. Here we assume the soil is initially at residual saturation, $s_i = s_{wr}$, so that $q(s_i) = 0$. The saturation above the wetting front, s_u, is determined implicitly by equating the rainfall to the unsaturated flux, $R = q(s_u)$, and given by

$$s_u = s(z_f) = k_{rw}^{-1}\left(\frac{\mu R}{\mathrm{k}(\phi(z_f))\rho g}\right), \tag{12}$$

where k_{rw}^{-1} is the inverse of the relative permeability. The speed of the wetting front, $\mathcal{S}_f$, changes with depth due to the competing effects of declining porosity, $\phi(z_f)$ and increasing saturation at the wetting front $s(z_f)$. The location and saturation of the wetting front are determined by solving the following ODE

$$\frac{\mathrm{d}z_f}{\mathrm{d}t} = \frac{R}{\phi(z_f)\,(s(z_f) - s_{wr})} \quad \text{with} \quad z_f(t=0) = 0. \tag{13}$$

Equation (13) can be integrated to get wetting front location $z_f(t)$ with time using analytical or numerical methods. This is valid until the wetting front becomes saturated, $s(z_f) = 1 - s_{gr}$. We refer to the corresponding location of the wetting front as the depth of saturation, z_s, which is given by

$$z_s = \phi^{-1}\left(\mathrm{k}^{-1}\left(\frac{\mu R}{k_{rw}^0 \rho g}\right)\right), \tag{14}$$

where ϕ^{-1} and k^{-1} are the inverse functions of the porosity and permeability. In addition, k_{rw}^0 is the end-point relative permeability of water phase, i.e., $k_{rw}^0 = k_{rw}(1 - s_{gr})$. The time of formation of the saturated region, t_s, is determined implicitly by integrating the inverse of (13) to obtain

$$t_s = \frac{1}{R}\int_0^{z_s} \phi(z_f)\,(s(z_f) - s_{wr})\mathrm{d}z. \tag{15}$$

This integral can be evaluated analytically or numerically. The first stage ends at t_s, after that a saturated region forms and the flow transitions to stage 2.

3.2 Stage 2 ($t_s \leq t < t_p$): Choking and formation of rising perched water table

After the wetting front reaches saturation at t_s, a finite-size saturated region, Ω_s, forms and grows with time (Figure 2*b*). The saturated flux, q_s, is equal to the harmonic mean of the hydraulic conductivity, $\bar{K}$, across the saturated region, see (8). Because K declines with depth, the saturated flux is always less than the incoming unsaturated flux, which is equal to the rainfall intensity, $q_u = R$. Therefore, the saturated region limits the infiltration at depth and a perched water table begins to form. We refer to this

phenomenon as *choking* and to the saturated region as a perched, but its base is the downward propagating wetting front instead of an aquitard (Cherry & Freeze, 1979).

The formation of the saturated region results in propagation of two shock fronts emanating from z_s that bound the growing saturated region, $\Omega_s(t)$. The lower boundary of the saturated region is the wetting front which continues to propagate downward. The upper boundary of the saturated region is the perched water table which propagates upward against the direction of infiltration. The propagation speeds of these two fronts can be determined from (10) and are respectively given by

$$\mathcal{S}_u = \frac{\mathrm{d}z_u}{\mathrm{d}t} = \frac{q_s - R}{\phi_u(1 - s_{gr} - s_u)} < 0, \tag{16}$$

$$\mathcal{S}_l = \frac{\mathrm{d}z_l}{\mathrm{d}t} = \frac{q_s}{\phi_l(1 - s_{gr} - s_{wr})} > 0, \tag{17}$$

where $\phi_l = \phi(z_l)$, $\phi_u = \phi(z_u)$ and s_u is the saturation above the perched water table. The shocks propagate in opposite directions, because both denominators are positive, but the numerator of (16) is negative, $q_s < R$, while the numerator of (17) is positive, $q_s > 0$. These shock speeds generally vary with time depending on the local RH jump conditions around the shocks. Therefore, the boundaries of the saturated region must be found by solving the system of coupled ordinary differential equations (16 & 17) for the locations of the upper $z_u(t)$ and lower boundaries $z_l(t)$ of the saturated region. The initial condition of the system is that both fronts originate from the location where the initial wetting front first saturates, $z_l(t_s) = z_u(t_s) = z_s$.

These derived relations are valid for general relative permeability k_{rw} variations with water saturation s. This theory is also valid even when the absolute permeability k is not a function of porosity ϕ but still varies with depth z. The time the upward moving shock takes to reach the surface after its formation is denoted by t_u and can be found by solving the system of ODEs until $z_u(t) = 0$. Therefore, the ponding time for this case is

$$t_p = t_s + t_u. \tag{18}$$

Once the water ponds on the surface, the rate of infiltration declines and the dynamics enter stage 3.

3.3 Stage 3 ($t \geq t_p$): Saturated gravity-driven infiltration

Once the perched water table, i.e., the upward moving back-filling shock, reaches the surface the rainfall begins to pond. The soil above the wetting front is now saturated and the dynamics are similar to the infiltration limited case (c) with instantaneous ponding, except that the wetting front is already located at $z_l(t_p)$. At the moment of ponding the infiltration rate drops instantaneously to the saturated flux, $q_s(t)$, and continues to decline as the wetting front penetrates deeper into the soil. In this stage, the infiltration is independent of the rainfall rate, R and is solely determined by the harmonic mean of the hydraulic conductivity of the saturated soil.

We assume that ponded water runs off instantaneously, so that the perched water table remains fixed at the surface, i.e., $\mathcal{S}_u = 0$ and $z_u = 0$. The saturated region within the soil continues to grow as the wetting front advances with speed $\mathcal{S}_l$, and its position can be obtained by integrating (17). The dynamics in this stage is determined by the evolution of the saturated flux (8), which is equal to the mean of the hydraulic conductivity, $\bar{K}$, above the wetting front. Because the porosity declines with depth the flux decreases continuously with time.

Below we illustrate these general principles with the application to three different specific porosity profiles with depth. This allows us to give specific front speeds, times of saturation and ponding as well as the evolution of the infiltration with time. These examples provide valuable test cases for numerical simulation of infiltration.

4 Examples

In this section we analyze three specific cases of porosity variation to illustrate the infiltration dynamics. Here we assume that both absolute permeability $\mathrm{k}(\phi)$ and the relative permeability of water $k_{rw}(s)$ follow power-laws (Brooks & Corey, 1964; Kozeny, 1927; Carman, 1937) and are given by

$$\mathrm{k}(\phi) = \mathrm{k}_0\phi^m, \quad k_{rw}(s) = k^0_{rw}s^n_e(s), \quad \text{so that} \quad K(\phi, s) = K_0\phi^m s^n_e(s) \tag{19}$$

where k_0, k^0_{rw} and $K_0 = \mathrm{k}_0 k^0_{rw}\rho g/\mu$ are model constants and s_e is the effective saturation defined as

$$s_e(s) = \frac{s - s_{wr}}{1 - s_{gr} - s_{wr}}. \tag{20}$$

With these constitutive relations and in absence of capillary forces the infiltration capacity is given by the saturated hydraulic conductivity at the surface, $f_c = K_0\phi(0)^m$. To non-dimensionalize these equations for sake of generality (Nachabe, 1996) the depth coordinate z is scaled with a characteristic depth z_0, time t is scaled with the characteristic time z_0/f_c, and infiltration rate (or volumetric flux) q is scaled with the infiltration capacity f_c. Therefore, the dimensionless variables are

$$z' = z/z_0, \quad t' = tf_c/z_0 \quad \text{and} \quad q' = q/f_c. \tag{21}$$

All results in this section are given in dimensionless form and all figures show analytical results unless mentioned otherwise. For the figures in this section we have chosen the power-law exponents as $m = 3$ and $n = 2$ and set the residual saturations to zero, i.e., $s_{wr} = s_{gr} = 0$. For all porosity profiles in this section we also provide comparisons with numerical solutions of the governing equations in the limit of no capillary forces (7 and 8). The details of this numerical solver are described in Shadab and Hesse (2022a).

Below, we first discuss the simple case of a two-layer soil with a discontinuous change in porosity, because it allows a detailed analysis that helps to build a physical understanding of the dynamics. In particular, it illustrates the mechanism of saturated layer formation and its growth due to the interaction with the surrounding unsaturated regions. Then we consider two common cases of continuous porosity decline which demonstrate the broad applicability of our results.

4.1 Discontinuous reduction in porosity

Consider a two layer dry soil with a decrease in porosity at z_0 from ϕ_u in the upper layer to ϕ_l in the lower layer (Figure 3*a*). The corresponding hydraulic conductivities are given by (19). We denote the partially saturated conductivities in the upper and lower layer as $K_u(s) = K(\phi_u, s)$ and $K_l(s) = K(\phi_l, s)$ and we refer to the saturated conductivities simply as K_u and K_l. In this two-layer case, the infiltration capacity is equal to the saturated conductivity of the upper layer, $f_c = K_u$. For the case of transitional infiltration, $K_u > R$, an unsaturated wetting front forms in the upper layer. Here we consider the case where $K_l \leq R$ so that a saturated region forms once the wetting front encounters the lower layer. The saturated region forms at the discontinuity,

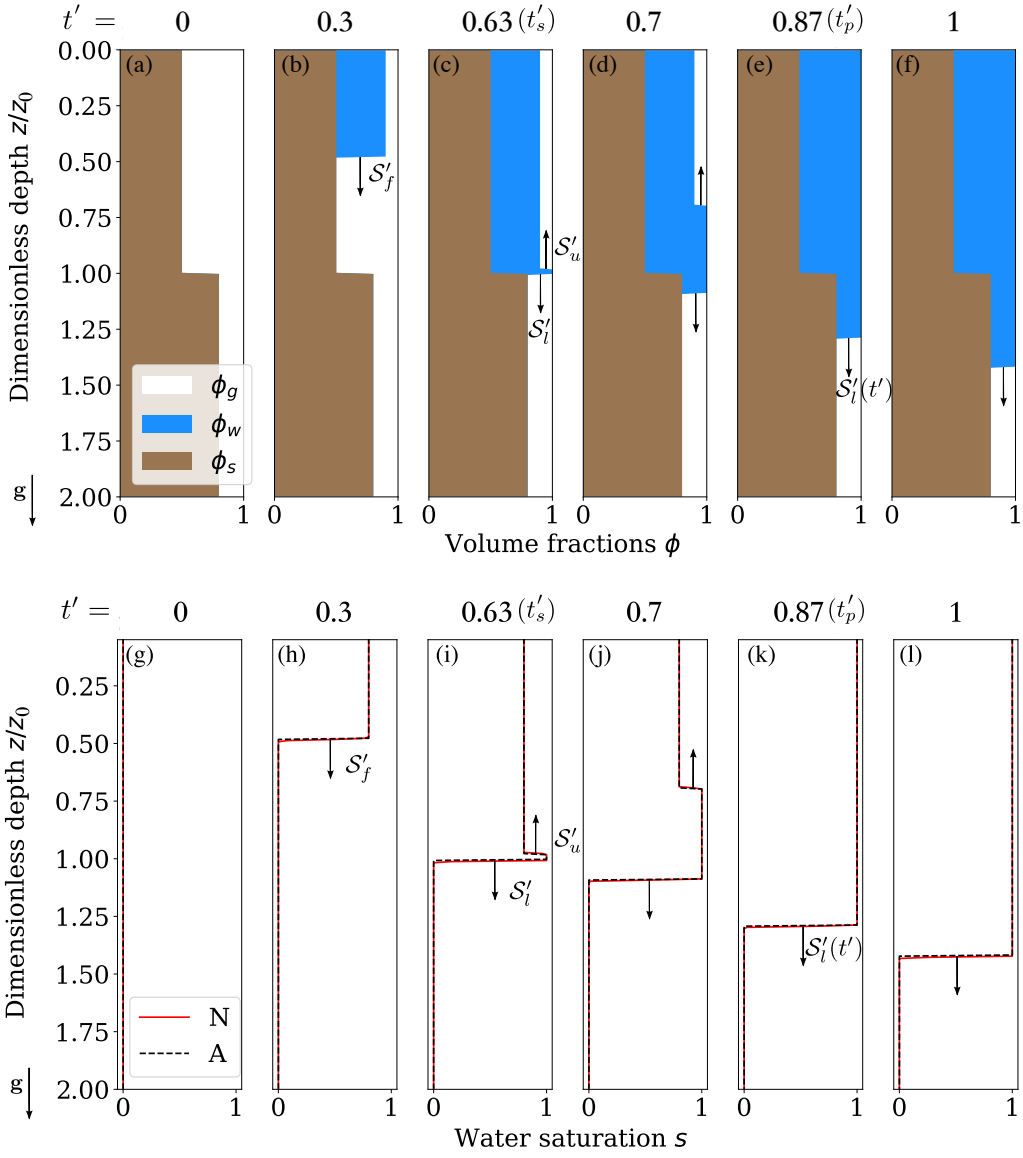

Figure 3: Infiltration process in an initially dry two-layered soil at different dimensionless times t' for $R/f_c = 0.64$, $\phi_u = 0.5$ and $\phi_l = 0.2$. Top row (a to f): Evolution of volume fractions in the dimensionless analytic solution, given in Section 4.1, where ϕ_g, ϕ_w and ϕ_s refers to gas, water (moisture content) and soil, respectively. Bottom row (g to l): Comparison of water saturation, s, between analytic solution (A) and the numerical solution (N) from Shadab and Hesse (2022a) with 400 uniform cells and a domain from 0 to 2.

$z_s = z_0$, and grows in both directions. In Figure 3 we show both the analytic solution developed below (3*a*-3*f*) and a comparison with a numerical solution (3*g*-3*l*).

Since the soil is initially at residual saturation, $s_i = s_{wr}$, the unsaturated wetting front during stage I moves downwards with constant velocity (Figure 3*b*). The shock velocity, $\mathcal{S}_f$, is given by (11) and can be visualized by the standard shock construction shown in Figure 4*a*, for details see Smith (1983) or Charbeneau (1984). From (13), the location of the wetting front is given by

$$z_f(t) = \frac{R\,t}{\phi_u\,(s_u - s_{wr})}, \qquad t \le t_s. \tag{22}$$

and the saturation behind the wetting front is

$$s = s_{wr} + (1 - s_{gr} - s_{wr})\left(\frac{R}{f_c}\right)^{1/n} \quad \text{for} \quad z \le z_f(t). \tag{23}$$

Once the initial front reaches the discontinuity at z_0 the domain saturates instantly and the time of saturation, t_s, is given by substituting $z_f = z_0$ into (22).

With the formation of the saturated region, $\Omega_s(t)$, the flow enters stage II (Figure 3*c* and 3*d*). The saturated region grows and is bounded by an upper and lower front, $z_u(t)$ and $z_l(t)$, that emanate from $z_s = z_0$. Their locations are given by the system of differential equations (16 & 17) with the initial condition $z_u(t_s) = z_l(t_s) = z_s$. The corresponding shock constructions are shown in Figure 4*b*. Due to the reduction in porosity, the unsaturated flux in the lower layer is smaller. In the extended kinematic wave approximation the shocks bounding the saturated region are given by chords between the flux functions in each layer and saturated flux, q_s.

The saturated flux, q_s, always lies in between the saturated limits of the flux functions in the two layers (Figure 4*b*), because it is the harmonic average over the saturated region. This implies that the formation of a saturated region always chokes the flow and that the two fronts bounding the saturated region must move in opposite directions. The formation of a saturated region therefore always leads to the formation of a rising perched water table. For a two layer soil, the expression for the saturated flux simplifies to the standard harmonic mean

$$q_s(t) = \frac{l(t)}{\frac{l_u(t)}{K_u} + \frac{l_l(t)}{K_l}}, \tag{24}$$

where the length of the saturated region in upper and lower layers are $l_u(t) = z_s - z_u(t)$ and $l_l(t) = z_l(t) - z_s$ respectively. The total length of the saturated region is $l(t) = l_u(t) + l_l(t) = z_l(t) - z_u(t)$. In general, the saturated flux is time-dependent, so that the velocities of the shocks bounding the saturated region can change with time, even if the change in saturation across the front remains constant. This is an important difference between the extended kinematic wave approximation and the standard kinematic theory where shock velocities are constant if the saturation change across the front is constant.

Although the saturated flux is generally time dependent, for the special case of a two layer soil the volumetric flux in the saturated region, q_s, remains constant until the perched water table reaches the surface, $t_s \le t \le t_p$. The saturated flux can be determined using the Ansatz that the ratio of shock speeds is constant

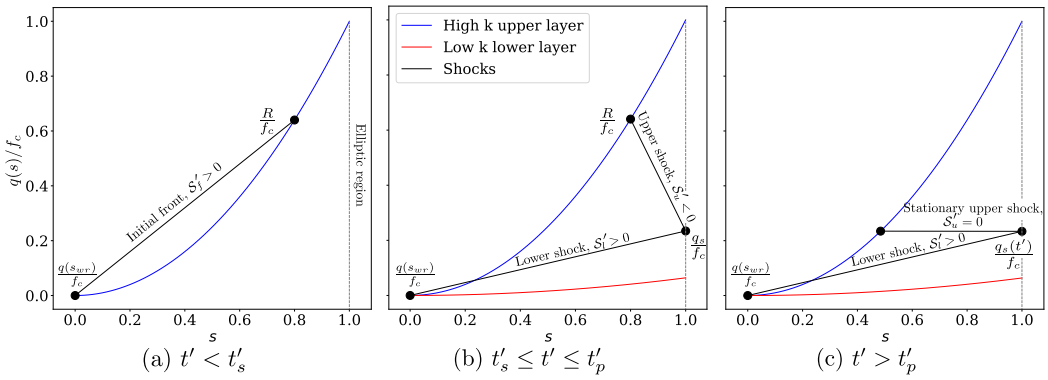

(a) $t' < t'_s$ (b) $t'_s \leq t' \leq t'_p$ (c) $t' > t'_p$

Figure 4: Shock constructions for the two-layer case shown in Figure 3 and discussed in Section 4.1. The flux function for the upper layer is shown in blue and the flux function for the lower layer is shown in red. (*a*) Stage I ($t' < t'_s$): Chord represents shock speed of the initial unsaturated wetting front. (*b*) Stage II ($t'_s \leq t' < t'_p$): Two chords connecting flux functions to q_s represent the speeds of the shocks bounding the saturated region and moving in opposite directions. (*c*) Stage III ($t' \geq t'_p$): Upper shock is stationary at surface (horizontal chord) and lower shock speed decreases as q_s declines over time.

$$\frac{\mathcal{S}_u}{\mathcal{S}_l} = \frac{z_u(t) - z_s}{z_l(t) - z_s} = \mathfrak{C}(s_u) \quad \text{for} \quad t_s \leq t \leq t_p. \tag{25}$$

This constant, $\mathfrak{C}$, depends only on the saturation of the initial wetting front, s_u. Substituting (16) and (17), $\mathfrak{C}$ is shown to be the solution of a quadratic equation

$$\begin{aligned} \mathfrak{C}(s_u) &= \frac{-b - \sqrt{b^2 - 4ac}}{2a}, \\ a &= \frac{\phi_u}{\phi_l}\left(\frac{1 - s_{gr} - s_u}{1 - s_{gr} - s_{wr}}\right), \\ b &= -\frac{\phi_u}{\phi_l}\left(\frac{1 - s_{gr} - s_u}{1 - s_{gr} - s_{wr}}\right) - \left(1 - \frac{K_u(s_u)}{K_u}\right), \\ c &= 1 - \frac{K_u(s_u)}{K_l}. \end{aligned} \tag{26}$$

The corresponding saturated flux q_s during $t_s \leq t \leq t_p$ is given by,

$$q_s = \frac{\mathfrak{C} - 1}{\mathfrak{C}/K_u - 1/K_l}, \tag{27}$$

and hence shown to be constant. Once q_s is known to be constant it follows from (16) and (17) that the shock speeds are constant for $t_s \leq t < t_p$. Therefore, the shock locations during stage II vary linearly with time.

As the upper shock reaches the surface at t_p the flow enters stage III (Figure 3*e* and 3*f*). For $t \geq t_p$, we assume that ponded water forms runoff so that the upper shock remains stationary the surface, $z_u(t) = 0$. The lower shock location $z_l(t)$ can then be evaluated by only integrating (17). Further, the saturated flux $q_s(t)$ becomes the infiltration rate $I(t) < R$, which can be evaluated from (24) by setting $l_u = z_0$. The corresponding shock constructions are shown in Figure 4*c*.

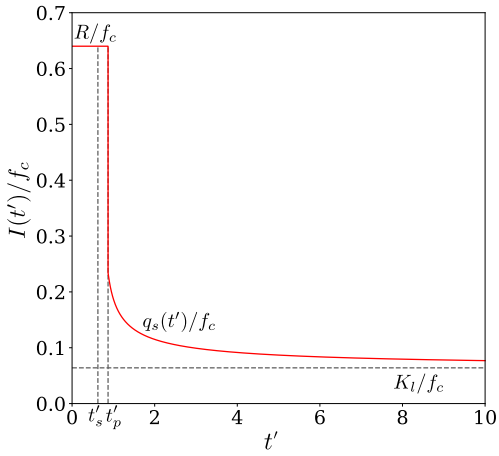

Figure 5: Evolution of the dimensionless infiltration rate $I(t')/f_c$ with t' for test shown in Figure 3.

The dimensionless infiltration rate I/f_c is equal to R/f_c before ponding, as shown in Figure 5. However, at the moment of ponding, the infiltration rate I/f_c drops instantaneously down to the value of the saturated flux q_s/f_c, while the reminder, $R/f_c - q_s/f_c$, forms runoff. Subsequently, the infiltration rate gradually drops and approaches the dimensionless saturated hydraulic conductivity of the lower layer, K_l/f_c. This happens because the effective hydraulic conductivity in the saturated region increasingly skews to the less conductive lower layer.

Because the solution is one-dimensional the entire evolution can be visualized in the $z-t$ plane (Figure 6). In the kinematic wave analysis the solution is constructed using characteristic curves along which water saturation propagates (LeVeque, 1992). In Figure 6*a* the gray lines are the characteristics and the colorful lines give the shock locations as function of time. In the unsaturated region, the governing equation (7-8) is hyperbolic and information propagates with finite characteristic speed. For any given saturation the speed of a characteristic is given by its slope as

$$\left.\frac{\mathrm{d}z'}{\mathrm{d}t'}\right|_s = \frac{\mathrm{d}q'(s)}{\mathrm{d}(\phi s)} = \frac{n}{\phi}\frac{(s-s_{wr})^{n-1}}{(1-s_{gr}-s_{wr})^n}. \tag{28}$$

For example, the soil is initially at residual saturation and the characteristics emanating from the left boundary are horizontal, indicating no transport of saturation. The characteristics entering the domain from above represent the infiltrating water ($t' \leq t'_p$) and hence have a finite slope carrying the water saturation at the surface down into the soil. In the saturated region, in contrast, the governing equation (7-8) is elliptic and information propagates instantaneously, as indicated by the vertical characteristics in Figure 6*a*.

Shock fronts in saturation form where characteristics with different slopes converge. The initial wetting front is shown in red and propagates into the soil with constant speed (Stage I). At t'_s, this initial front bifurcates into two fronts (black and blue) moving in opposite directions that bound the saturated region (Stage II). The blue line represents the rising perched water table which reaches the surface at t'_p. The black line shows the continued downward propagation of the wetting front, which gradually slows down after ponding occurs (stage III).

The characteristics shown in Figure 6*a*, trace the propagation of the water saturations in the soil. These do not correspond to the paths of physical water particles. For

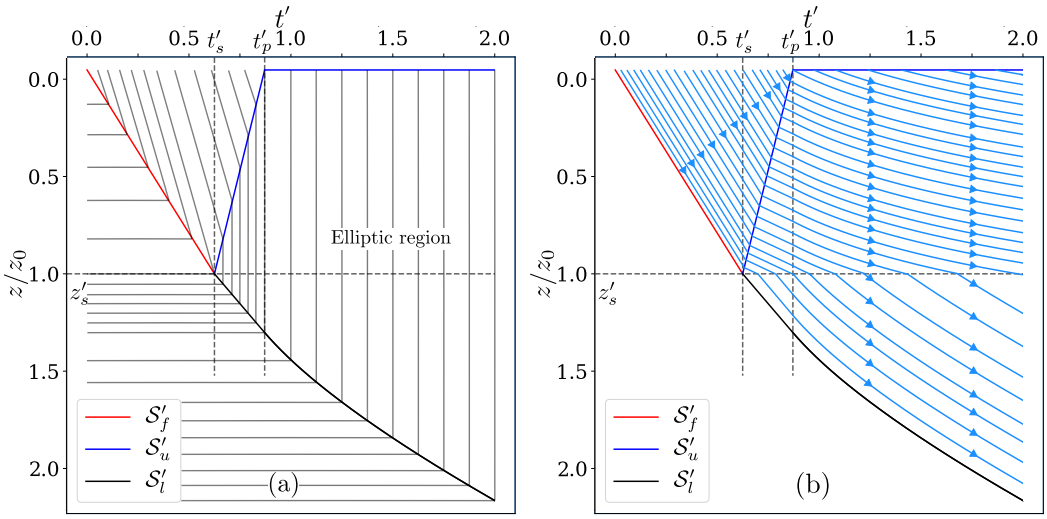

Figure 6: Characteristics and fluid particle paths for the two-layer case shown in Figure 3. Here horizontal axis refers to the dimensionless time t' whereas the vertical axis refers to dimensionless location (z/z_0). Red, blue and black lines refer to the initial front, upper and lower shocks respectively. (a) The characteristic diagram where grey lines are the characteristics corresponding to flow of the information. (b) The fluid particle path diagram where light blue lines are the particle paths correspond to location of water parcel after entering the soil. The characteristics in the elliptic region are vertical (and imaginary) as information propagates at infinite speeds.

example, although the perched water table is rising, the direction of water flow is always downward. The particle paths are shown in Figure 6b and can be obtained by integrating the dimensionless interstitial velocity of the water phase, $u'_p = q'(s,t)/\phi s$. Any water parcel that enters the soil before ponding initially percolates at a constant interstitial velocity equal to the speed of the wetting front (Stage I). Once it crosses the rising perched water table (dark blue), its velocity decreases due to the reduced water flux in the saturated region (Stage II). After ponding ($t' \geq t'_p$), the trajectories become curved due to the gradual reduction of the saturated flux with time which reduces the percolation velocity (Stage III). Water parcels that enter the lower layer experience an increase of velocity because the saturated flux is constant but the porosity in the lower layer is smaller.

In Figure 7 we explore the effect of rainfall rate and porosity in the lower soil on the evolution of the infiltration rate. By increasing the dimensionless rainfall rate R/f_c from 0.2 to 0.9 for fixed $\phi_l = 0.2$ and $\phi_u = 0.5$, it can be observed from Figure 7a that the ponding time t'_p reduces from 3.97 to 0.58, as the perched water table rises faster due to the three cumulative effects. First, the initial wetting front is faster since the rainwater flux is higher which shortens the time of saturation (t_s). Second, due to lower gas saturation behind the initial front the back-filling is faster. Third, the excess volumetric flux at the jump accumulates in the rising perched water table, leading to a faster back-filling. These three effects cumulatively lead to a shorter ponding time when the rainfall rate is increased. The instantaneous drop in the infiltration rate at the time of ponding becomes larger with increasing rainfall rate, as indicated from the black dots. At large times all the curves asymptotically converge to the dimensionless hydraulic conductivity of lower soil K_l/f_c. These reductions in infiltration lead to corresponding increases in runoff not shown in the graph.

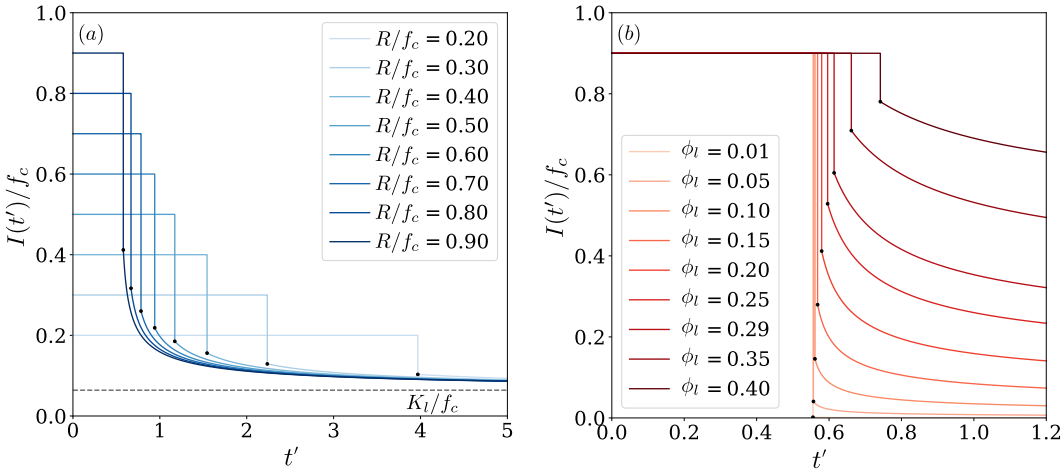

Figure 7: Evolution of dimensionless infiltration rates in an initially dry two-layered soil with varying rainfall rate or lower layer porosity and fixed upper layer porosity $\phi_u = 0.5$. (a) Effect of varying the dimensionless rainfall rates R/f_c with constant lower layer porosity $\phi_l = 0.2$. (b) Effect of varying the lower soil porosity ϕ_l and keeping the dimensionless rainfall rate $R/f_c = 0.9$ fixed.

Figure 7b shows the effect of increasing the porosity of the lower soil from $\phi_l = 0.01$ to 0.4 for a constant rainfall rate $R/f_c = 0.9$. In this case, the time of saturation is constant, $t'_s = 0.53$, but the time of ponding increases from 0.56 to 0.74, as shown by the black dots. Thus, the rise in the perched water table is slower if the lower layer is more porous and accommodates a larger fluid flux. The instantaneous drop in the infiltration rate at the time of ponding increases with decreasing porosity in the lower layer. The asymptotic infiltration rates increase with the porosity and hydraulic conductivity in the lower soil layer.

The simple case of a layered soil is valuable because it allows detailed analysis that informs our understanding of the dynamics of the formation and evolution of the saturated region and its interaction with the ambient unsaturated flow. A particular feature of this case is that the saturated flux remains constant as long as the saturated region does not interact with the boundary of the domain. This preserves the self-similarity of the solution in z/t which allows the full application of the tools from the kinematic wave analysis or more broadly the analysis of hyperbolic conservation laws (LeVeque, 1992). This extension of kinematic wave analysis is remarkable, because the governing equation becomes elliptic in the saturated region. Below we will explore more complicated cases with continuously varying porosity where the saturated flux always varies with time.

4.2 Exponential reduction in porosity

The porosity and/or hydraulic conductivity of soils generally decline with depth (Childs & Bybordi, 1969) and are often fit as exponential decay functions (Beven, 1984). More recently Meyer and Hewitt (2017) considered a similar porosity decay for infiltration into firn, i.e., sintered and compacted snow. Here we consider such an exponential decay in soil porosity with depth, given by

$$\phi(z) = \phi_0 e^{-z/z_0}, \tag{29}$$

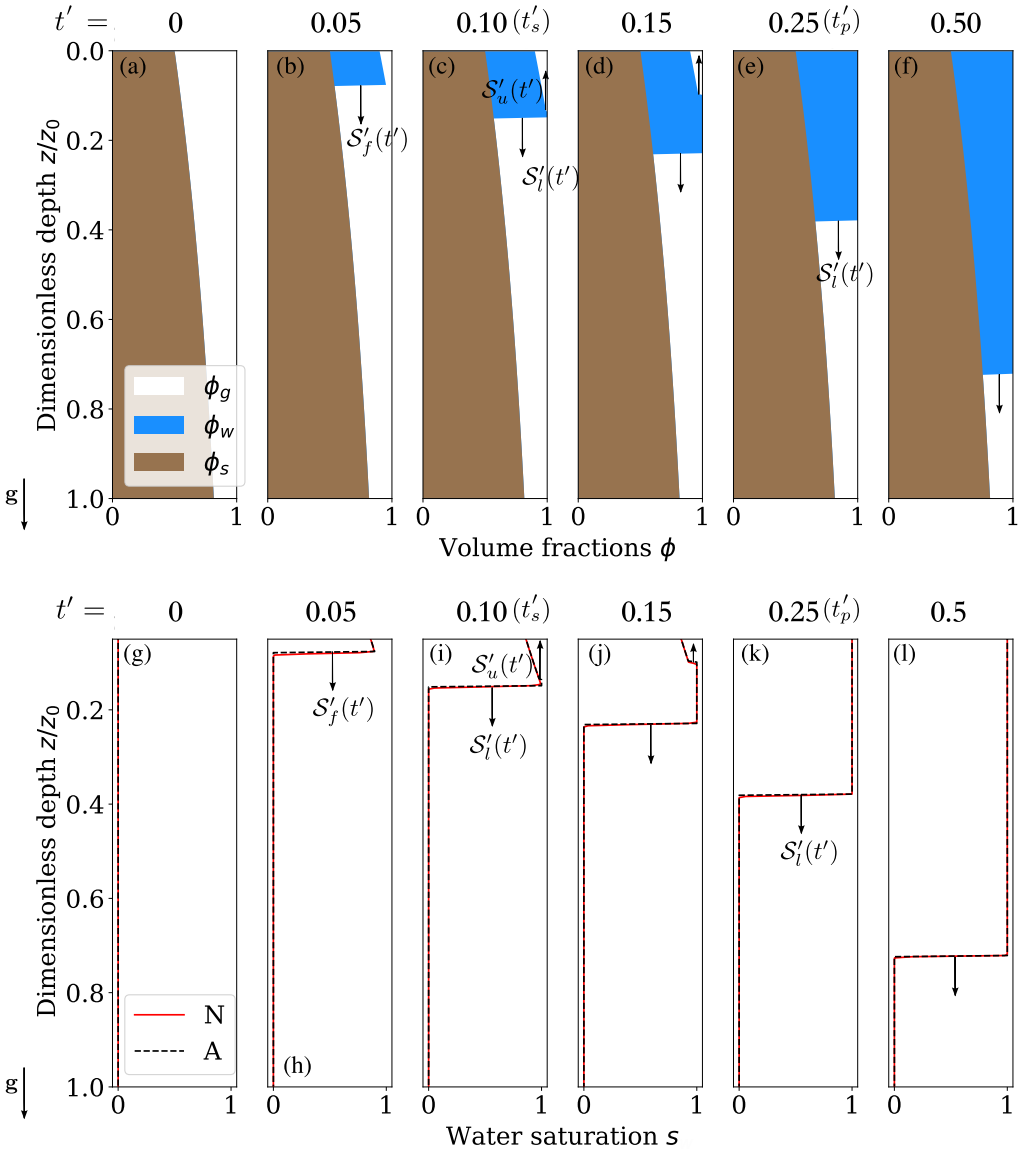

Figure 8: Infiltration process in an initially dry soil with exponential reduction in porosity shown at different dimensionless times t' for $R/f_c = 0.64$ and $\phi_0 = 0.5$. Top row (a to f): Evolution of volume fractions in the dimensionless analytic solution, given in Section 4.1, where ϕ_g, ϕ_w (moisture content) and ϕ_s refers to gas, water and soil, respectively. Bottom row (g to l): Comparison of water saturation, s, between analytic solution (A) and the numerical solution (N) from Shadab and Hesse (2022a) with 400 uniform cells and a domain from 0 to 1.

where ϕ_0 is the porosity at the surface $z = 0$ and z_0 is a characteristic depth (Figure 8*a*). The corresponding hydraulic conductivity is given by (19) and the infiltration capacity is the hydraulic conductivity at the surface, $f_c = K_0\phi_0^m$. For an exponential porosity decay any rainfall with $R < f_c$ is transitional, because K asymptotically approaches zero with increasing depth.

This specific solution can be constructed by specializing the general results derived in Section 3 to the porosity decay given by (29). Initially an unsaturated wetting front forms (Stage I), but its saturation continuously increases with depth as porosity declines (Figure 8*b*). The saturation at the shock can be obtained from (12) and is given by

$$s(z_f) = s_{wr} + (1 - s_{gr} - s_{wr}) \left(\frac{R}{f_c}\right)^{1/n} e^{mz_f/nz_0}. \tag{30}$$

The location of the initial wetting front is then obtained by substituting (29) and (30) into (13) and given by

$$z_f(t) = \frac{n}{m-n} z_0 \ln\left(1 + \frac{m-n}{n} \frac{R}{\phi_0 z_0} \frac{\sqrt[n]{f_c/R}}{(1 - s_{gr} - s_{wr})} t\right). \tag{31}$$

The continued increase in saturation at the wetting front eventually leads to the formation of a saturated region (Figure 8*c*). The depth where the saturated region initially forms, z_s, is obtained from (14), and given by

$$z_s = \frac{z_0}{m} \ln\left(\frac{f_c}{R}\right). \tag{32}$$

The time of saturation, t_s, is then obtained by equating (32) with (31) and given by

$$t_s = \frac{n}{m-n} \frac{\phi_0 z_0}{R} (1 - s_{gr} - s_{wr}) \left[\left(\frac{R}{f_c}\right)^{\frac{1}{m}} - \left(\frac{R}{f_c}\right)^{\frac{1}{n}}\right]. \tag{33}$$

After the formation of the saturated region, $\Omega_s(t)$, the flow enters stage II. The growing saturated region is bounded between the rising perched water table, $\mathcal{S}_u$, and the wetting front that continues to propagate downward, $\mathcal{S}_l$ (Figure 8*d*). The flux in the saturated region is given by the harmonic mean (9) of the hydraulic conductivity over the saturated region, which becomes

$$q_s(t) = \overline{K} = \frac{mf_c}{z_0} \frac{(z_l(t) - z_u(t))}{e^{mz_l(t)/z_0} - e^{mz_u(t)/z_0}}. \tag{34}$$

The speeds and locations of the two fronts bounding the saturated region cannot be obtained analytically and require numerical integration. For the downward moving lower shock, the shock speed $\mathcal{S}_l$ can be calculated directly from (17) and the location of the wetting front is obtained by its coupled numerical integration. Since the Darcy flux in the upper region is fixed by rainfall rate R, the saturation s_u in the region right above the upper shock $z_u(t)$, is still the saturation of the initial front, $s_u(z_u) = s(z_f)$, given by (30). Substituting $s_u(z_u)$ into (16) gives the upper shock speed $\mathcal{S}_u$ as

$$\mathcal{S}_u = \frac{\mathrm{d}z_u}{\mathrm{d}t} = \frac{R - q_s}{\phi_u(1 - s_{gr} - s_{wr}) \left[\left(\frac{R}{f_c}\right)^{1/n} e^{mz_u/nz_0} - 1\right]}, \tag{35}$$

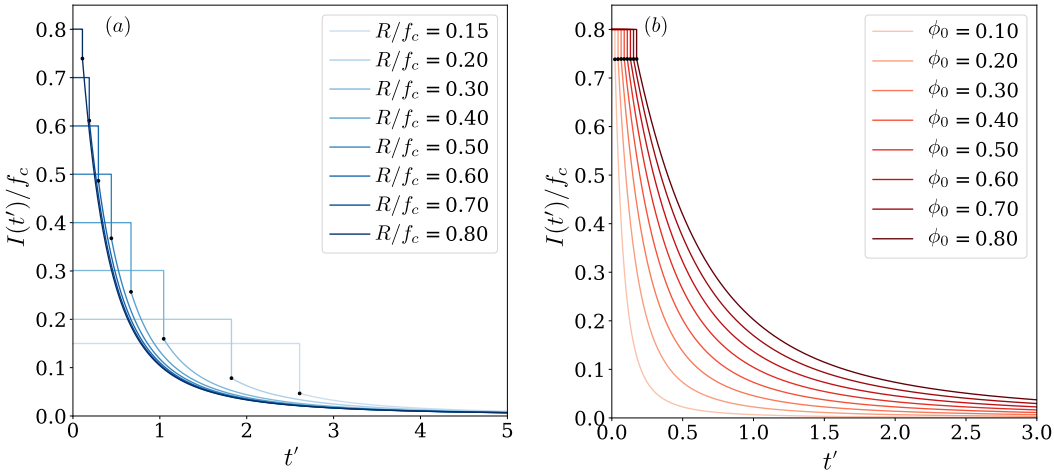

Figure 9: Evolution of dimensionless infiltration rates $I(t')/f_c$ in an initially dry soil with porosity decreasing exponentially with depth. (a) Varying the dimensionless rainfall rates R/f_c. The porosity at the surface $\phi_0 = 0.5$ is fixed. (b) Varying the porosity at the surface ϕ_0 while keeping the dimensionless rainfall rate $R/f_c = 0.8$ fixed.

and the location of the perched water table, z_u, is obtained by its coupled numerical integration along with (17).

Once the perched water table reaches the surface the flow enters stage III and the wetting front continues to propagate into ever lower porosity soil at depth (Figure 8*e*-8*f*). As before, the infiltration rate drops instantaneously at the time of ponding and continues to decline towards zero afterwards. Figure 9 illustrates the effect of rainfall rate and surface porosity on the evolution of the infiltration rate. Figure 9*a* shows that increasing the dimensionless rainfall rate R/f_c from 0.15 to 0.80 at fixed $\phi_0 = 0.5$, decreases t'_p from 2.61 to 0.11. An interesting aspect of declining porosity with depth is that the largest drop in the dimensionless infiltration rate, I/f_c, at t'_p occurs for intermediate rainfall rates, $R/f_c \sim 0.3{-}0.5$. At low rainfall rates this drop is small because the flux is small and the wetting front has already reached very low porosity soil at the time of ponding. At high rainfall rates the flux is high but the drop is also small, because ponding occurs early while the wetting front is still in high porosity near-surface soil which has a high hydraulic conductivity. For all rainfall rates the dimensionless infiltration rates converge for $t' \sim 5$ and decline to zero asymptotically. Figure 9*b* shows the effect of increasing the surface porosity ϕ_0 from 0.1 to 0.8 at a fixed rainfall rate $R/f_c = 0.8$. Increasing ϕ_0 increases the ponding time, t'_p, from 0.02 to 0.18 but the instantaneous drop in I/f_c at t'_p increases only slightly. Although the drop at t'_p is almost constant, the subsequent decline in I/f_c is much more rapid if ϕ_0 is small. Finally, we note that changing ϕ_0 affects f_c, so that dimensional infiltration rates, I, will show large differences, although the initial dimensionless infiltration rate, I/f_c, shown in Figure 9*b* is constant.

Here we have applied the extended kinematic theory from Section 3 to more realistic exponentially declining porosity profiles. Though this requires numerical integration the solutions can be obtained quickly and accurately. A comparison of theses semi-analytical solutions with numerical solutions in Figure 8*g*-8*l* shows good agreement in all three stages of the flow. For the specific case of $m = 3$ and $n = 2$ our results reduce to those given in Meyer and Hewitt (2017).

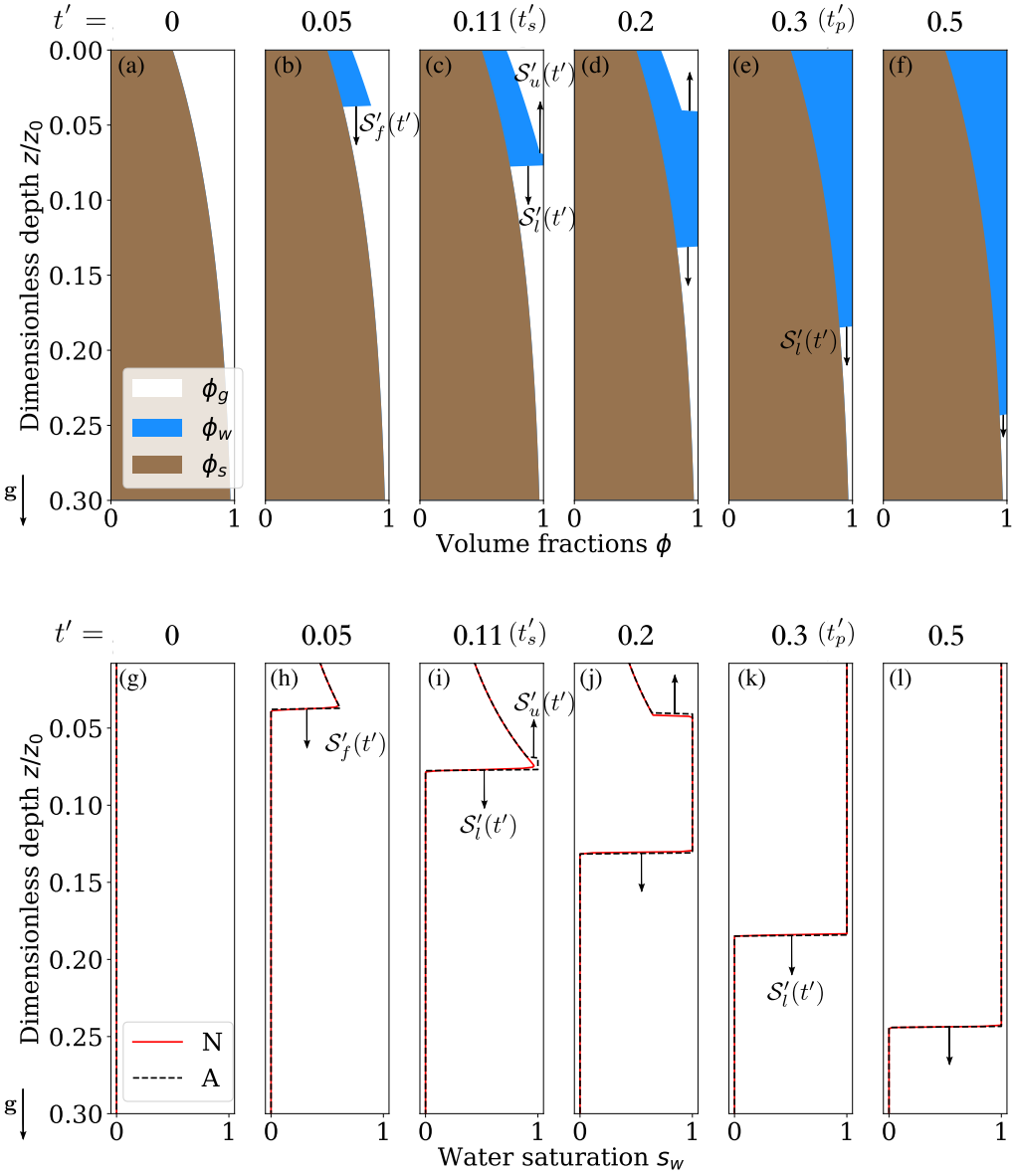

Figure 10: Infiltration process in an initially dry soil with power-law reduction in porosity shown at different dimensionless times t' with p $= 7.63$, $R/f_c = 0.64$ and $\phi_0 = 0.5$. Top row (a to f): Evolution of volume fractions in the dimensionless analytic solution, given in Section 4.3, where ϕ_g, ϕ_w (moisture content) and ϕ_s refers to gas, water and soil, respectively. Bottom row (g to l): Comparison of water saturation, s, between analytic solution (A) and the numerical solution (N) from Shadab and Hesse (2022a) with 400 uniform cells and a domain from 0 to 0.3.

4.3 Power law reduction in porosity

Many studies also consider soils with a porosity decay following a power law (Beven, 1982; Rupp & Selker, 2005), given by

$$\phi(z) = \phi_0(1 - z/z_0)^{\mathrm{p}} \tag{36}$$

where ϕ_0 is the constant porosity at the surface, z_0 is the depth of the impermeable bedrock where $\phi = 0$ and p is the power-law exponent (Figure 10a). The finite depth of the soil and hence the finite pore volume are the biggest differences relative to the exponential decay considered in Section 4.2. For high values of p, the reduction of porosity with depth is much faster than that for the exponential case discussed previously. Here the infiltration capacity is again $f_c = K_0\phi_0^m$, due to the absence of capillary forces. Similar to the exponential case, for a power law porosity decay any rainfall $R < f_c$ is transitional because $K \to 0$ as $z \to z_0$. The dynamics is quite similar to the exponential case discussed in Section 4.2.

In stage I, a wetting front moves downward with continuously increasing saturation (Figure 10b). The saturation at the shock can be obtained from (12) as

$$s(z_f) = s_{wr} + (1 - s_{gr} - s_{wr})\left(\frac{R}{f_c}\right)^{1/n}\left(1 - \frac{z}{z_0}\right)^{-\frac{m\mathrm{p}}{n}}. \tag{37}$$

Thus, the location of the wetting front is obtained by substituting (36) and (37) in (13) and given by

$$z_f(t) = z_0 - z_0\left[1 - \frac{-m\mathrm{p} + n\mathrm{p} + n}{n}\frac{R}{\phi_0 z_0(1 - s_{gr} - s_{wr})\left(\frac{R}{f_c}\right)^{1/n}}t\right]^{\frac{n}{-m\mathrm{p}+n\mathrm{p}+n}}. \tag{38}$$

Again the continuously increasing saturation at the wetting front leads to the formation of a saturated region (Figure 10c). The depth where this occurs is also obtained from (14) as

$$z_s = z_0\left(1 - \left(\frac{R}{f_c}\right)^{\frac{1}{m\mathrm{p}}}\right) \tag{39}$$

and the corresponding time of saturation is given by

$$t_s = \frac{n}{-m\mathrm{p} + n\mathrm{p} + n}\frac{\phi_0 z_0}{R}(1 - s_{gr} - s_{wr})\left[\left(\frac{R}{f_c}\right)^{1/n} - \left(\frac{R}{f_c}\right)^{\frac{\mathrm{p}+1}{m\mathrm{p}}}\right]. \tag{40}$$

Once the saturated region, $\Omega_s(t)$, has formed the flux in the saturated region is given by the continuous harmonic mean (9) of hydraulic conductivity in the saturated region and can be written as

$$q_s(t) = \overline{K}(t) = (m\mathrm{p} - 1)\frac{(z_l(t)/z_0 - z_u(t)/z_0)}{(1 - z_l(t)/z_0)^{-m\mathrm{p}+1} - (1 - z_u(t)/z_0)^{-m\mathrm{p}+1}}f_c. \tag{41}$$

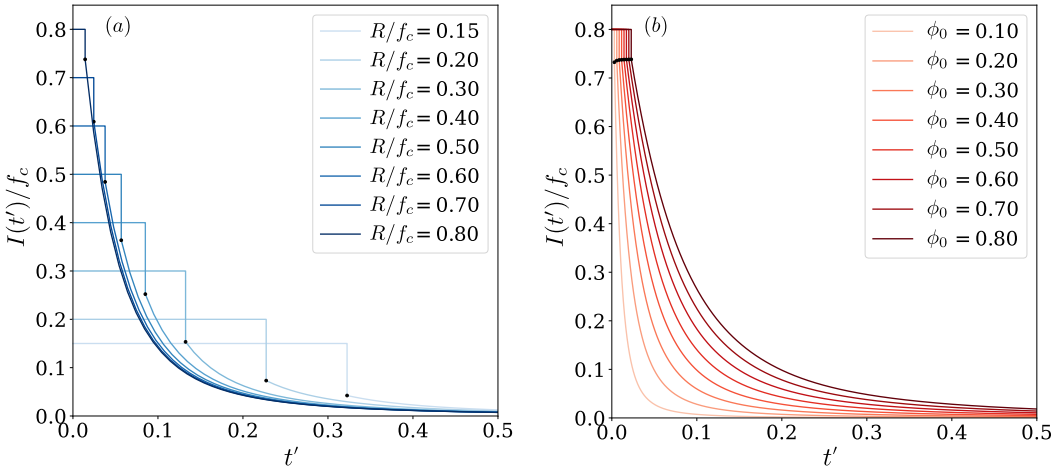

Figure 11: Evolution of dimensionless infiltration rates $I(t')/f_c$ in an initially dry soil with porosity decreasing as a power-law with depth for p $=$ 7.63, R/f_c $=$ 0.64 and ϕ_0 $=$ 0.5. (a) Varying the dimensionless rainfall rates R/f_c. The porosity at the surface ϕ_0 $=$ 0.5 is fixed. (b) Varying the porosity at the surface ϕ_0 while keeping the dimensionless rainfall rates $R/f_c = 0.8$ fixed.

The location of the downward moving lower shock, z_l, is given directly by numerical integration of the shock speed, $\mathcal{S}_l$, given by (17). To obtain the location of the perched water table, z_u, the saturation profile given by (37) must be substituted for s_u in the expression for the upper shock speed

$$\mathcal{S}_u = \frac{\mathrm{d}z_u}{\mathrm{d}t} = \frac{R - q_s}{\phi_u(1 - s_{gr} - s_{wr})\left[\left(\frac{R}{f_c}\right)^{1/n}(1 - z_u/z_0)^{-\frac{m\mathrm{p}}{n}} - 1\right]}. \tag{42}$$

The location of the perched water table, z_u, is then obtained by its coupled numerical integration along with (17).

Once the perched water table reaches the surface the flow enters stage III and the wetting front continues to propagate into ever lower porosity soil at depth (Figure 10*e*-10*f*). As before the dimensionless infiltration rate drops instantaneously at t'_p followed by an gradual decline toward zero. Figure 11 illustrates the effect of rainfall rate and surface porosity on the evolution of the infiltration rate. In both cases the evolution of I/f_c is remarkably similar to the exponential case (Figure 9), but the timescales are an order of magnitude faster, due to the more rapid porosity decay in the power-law case. We also provide a comparison of our semi-analytic solution with numerical solution for the power-law case in Figure 10*g*-10*l* and observe excellent agreement in all three stages of the flow.

5 Discussion

5.1 Infiltration in two-layered soil with Hydrus-1D

In Figures 3, 8 and 10 we have provided comparisons between our semi-analytic solution and numerical solutions of the governing equation in the limit of no capillary forces (7-8) as provided by (Shadab & Hesse, 2022a). Here we provide additional validation by comparison with a numerical solution to the full Richards equation, provided

Table 2: Summary of hydraulic properties of upper and lower layers for modified van-Genuchten model (Vogel & Cislerova, 1988) in Hydrus-1D (Šimunek et al., 2012)

Layer	Qr	Qs	$Alpha$ (1/cm)	n	K_s (cm/day)	l	Qm	Qa	Qk	K_k (cm/day)
Upper	0	0.43	0.5	2.68	106.1	0.5	0.43	0	0.43	106.1
Lower	0	0.1	0.5	2.68	1.33447	0.5	0.1	0	0.1	1.33447

by Hydrus-1D (Šimunek et al., 2012). For this comparison we choose the two-layer porosity profile discussed in Section 4.1. The Hydrus-1D simulation domain $[0, -100$ cm$]$ is discretized into 400 cells of equal size and run until a maximum time of 0.70688 days. The domain has a jump in porosity and hydraulic conductivity at $z_0 = -50$ cm, and the properties are summarized in Table 2.

For the Hydrus simulations we use the modified van-Genuchten model (mvG), because the suction head derivatives $\mathrm{d}\Psi/\mathrm{d}s$ remain bounded when $s \to 1$, which is necessary for convergence in presence of a saturated region (Vogel & Cislerova, 1988). The parameters for mvG model are also given in Table 2 and chosen so that upper and lower layers correspond to sandy-loam and silty clay loam (Carsel & Parrish, 1988), respectively. The $Alpha$ and n parameters of the mvG model (Vogel & Cislerova, 1988) in the Hydrus software (Šimunek et al., 2012) are chosen to reduce the capillary pressure effects to a minimum. The upper (surface) boundary condition is atmospheric with surface runoff whereas the lower boundary condition is free drainage. The precipitation R is 42.44 cm/day which makes $R/f_c = 0.4$ as $f_c = 106.1$ cm/day from Table 2. The initial head inside the domain is -100 cm.

The need to use the mvG model in Hydrus leads to a discrepancy with our analytic model which is based on the Brooks-Corey model for hydraulic properties. However, due to the simplicity of the solution the hydraulic properties are only sampled at the saturation of the initial wetting front, in addition to the dry and fully saturated states. This allows us to choose the parameters in the Brooks-Corey model to match the hydraulic conductivity at the front saturation as shown in Figure 12. The fitted Kozeny-Carman parameter is $m = 3$ and Brooks-Corey parameter is $n = 7.15306$ for the upper and lower layer porosities of 0.43 and 0.1 respectively.

The Hydrus simulation results are non-dimensionalized according to (21) and shown in Figure 13 together with the analytic solution from Section 4.1 and the numerical solution in the limit of no capillary forces from (Shadab & Hesse, 2022a). The agreement with the analytic solution is excellent in all three stages of the flow, but the fronts in the Hydrus solution are less sharp due to the presence of capillary forces which provide an additional diffusive water flux. The evolution of the infiltration rate is compared in Figure 14 and we observe an excellent agreement between Hydrus simulation and the analytic solution.

5.2 Comparison with experimental data and the effect of capillary suction

We are not aware of an experimental data set for transitional infiltration into a soil with a decrease in porosity that chokes the flow and leads to ponding. Instead, we provide a comparison with experiments by Childs and Bybordi (1969) that are infiltration limited, so that ponding occurs instantaneously, $t_p = 0$. As such their experiment corresponds to stage III in our dynamics and hence we refer to the location of the wetting front as z_l. Their soil comprises six layers of decreasing grain size, so that the hydraulic conductivity decays with depth but the porosity remains approximately constant (Ta-

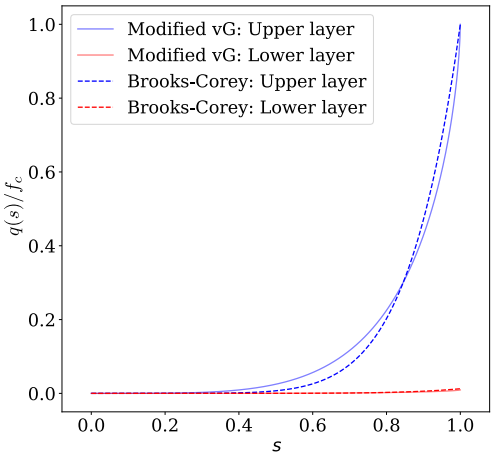

Figure 12: Variation of the dimensionless flux $q(s)/f_c$ (or $k_{rw}(s)$) with water saturation s for the two-layered test. Modified van-Genuchten and Brooks-Corey models are shown for highly conductive upper layer and less conductive lower layer.

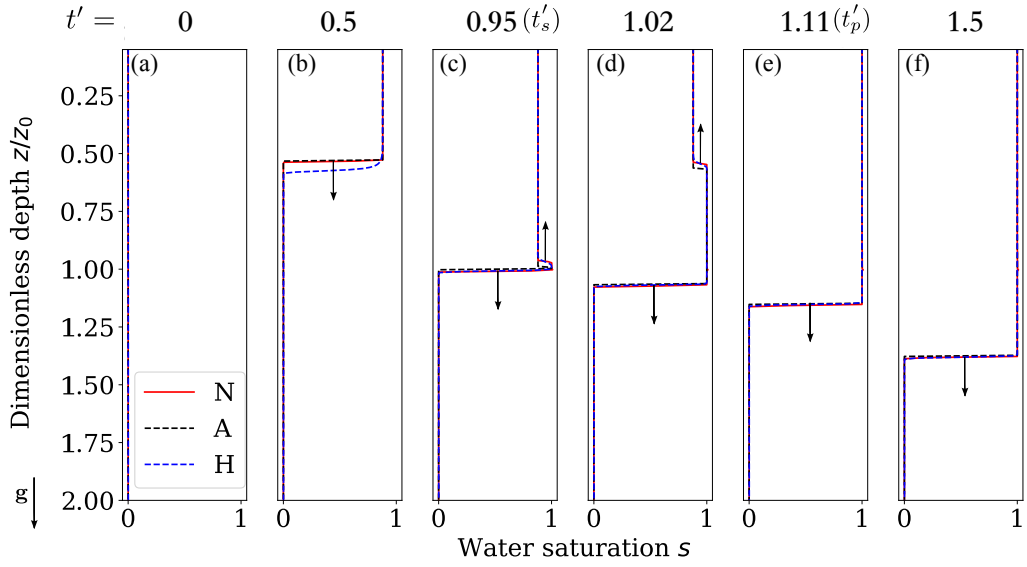

Figure 13: Infiltration process in an initially dry two-layered soil with $m = 3, n = 7.15306$ and no residual saturations shown at different dimensionless times t'. The porosities $\phi_u = 0.43$, $\phi_l = 0.1$ and $R/f_c = 0.4$ are fixed. The Y axis refers to the dimensionless depth (z/z_0) whereas the x axis refers to the water saturation s. 'N', 'A' and 'H' refer to the numerical, analytical and Hydrus solutions respectively. The dimensionless time is $t' = tf_c/z_0$.

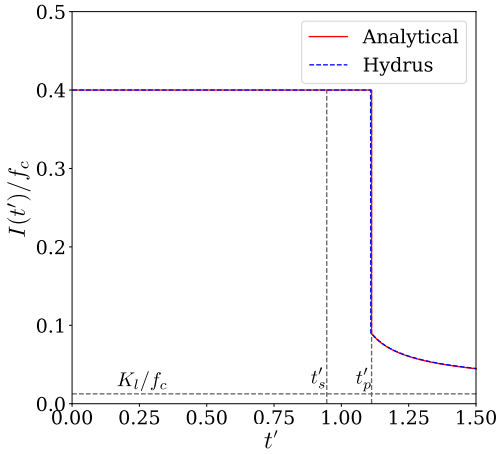

Figure 14: Evolution of dimensionless infiltration rate $I(t')/f_c$ with dimensionless time $t' = tf_c/z_0$ for test case shown in Figure 13.

Table 3: Data from Childs and Bybordi (1969) as given in Beven (1984). Each soil layer has been characterized by a saturated hydraulic conductivity K_s, a Green and Ampt wetting front potential Ψ_{wf} and the available pore space $\Delta\theta$, which can be considered as the $\Delta\theta = \phi(1 - s_{gr} - s_{wr})$.

Layer (m)	K_s (m/h)	Ψ_{wf} (m)	$\Delta\theta$
0–0.3	13.2	-0.06	0.35
0.3–0.6	7.5	-0.08	0.3355
0.6–0.9	4.2	-0.1	0.36
0.9–1.2	2.9	-0.125	0.36
1.2–1.5	1.7	-0.159	0.365
1.5–1.8	0.5	-0.178	0.37

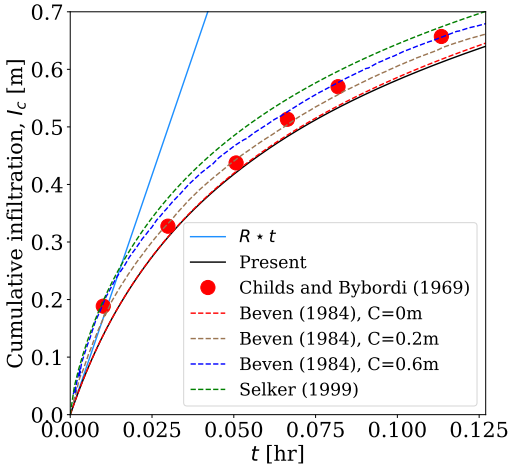

Figure 15: Infiltration in sand with exponentially reducing hydraulic conductivity and almost constant porosity with depth. The results shown the (semi-) analytical values for different models along with experimental results from Childs and Bybordi (1969).

ble 3). Following previous work by Beven (1984) and Selker et al. (1999) we fit the conductivity data with an exponential decay

$$K = K_o \exp(fz), \tag{43}$$

where $K_o = 16.65$ (m/hr) is the saturated hydraulic conductivity at the surface and $f = 1.888$ m^{-1} is the decay coefficient, where we have taken the values from Beven (1984).

The experiments of Childs and Bybordi (1969) provide data for the location of the wetting front, z_l. Because the porosity is constant the wetting front is directly related to the cumulative infiltration, given by

$$I_c = \int_0^{z_l} \Delta\theta \mathrm{d}z = \int_0^{z_l} \phi(1 - s_{wr} - s_{gr})\mathrm{d}z = \phi(1 - s_{wr} - s_{gr})z_l \tag{44}$$

where $\Delta\theta = \phi(1 - s_{wr} - s_{gr})$ is the available pore space. The cumulative infiltration data of Childs and Bybordi (1969) are shown in Figure 15.

We have developed the kinematic theory for exponential decay in soil properties in Section 4.2. However, we assume that ϕ decays exponentially and that K is a power-law of ϕ. To adapt our solution to this case we set the porosity exponent m to an arbitrarily high value ($m = 100$) so that $\phi = \phi_0 \exp(-fz/m)$ and is scaled out from hydraulic conductivity formulation. Using the values from Beven's model the infiltration capacity is $f_c = 16.65$ m/hr and the characteristic depth, $z_0 = -m/f = 100/1.888 = 52.97$ m is very large, which keeps the porosity constant, $\phi \approx \phi_0$. With these adjustments, the cumulative infiltration for stage III from our kinematic theory is shown in Figure 15. The kinematic theory captures the general trend very well, but underestimates the cumulative infiltration by approximately 6% at late time. This is partially due to fitting the six soil layers with a continuous exponential decay, but also reflects that capillary suction is neglected in the kinematic theory (Smith, 1983; Charbeneau, 1984; Milly, 1988).

At this point it is instructive to compare our results to previous studies modeling this data with extensions of the theory developed by Green and Ampt (1911) to soils with decaying porosity (e.g., Beven (1984); Selker et al. (1999)). One important difference between kinematic wave theory and Green-Ampt theory is that the latter includes a cap-

illary suction head, Ψ, in Darcy's law

$$q = -K\frac{\mathrm{d}h}{\mathrm{d}z} = -K\frac{h_0 - h_l}{z_l} = -K\frac{h_0 - (-\Psi - z_l)}{z_l} \approx -K\frac{\Psi + z_l}{z_l}, \tag{45}$$

where $h_0 = 0$ is the head at the surface and the head at the wetting front, $h_l = -\Psi - z_l$, is split into a capillary and elevation head (Te Chow, 2010). From (45) we see that the flux q is dominated by the capillary head for small z_l and by elevation head for large z_l. In the simplest case, Ψ, is assumed to be constant and results for increasing storage suction factor, $C = \Delta\theta\Delta\Psi$, from (Beven, 1984) are shown in Figure 15. Increasing capillary suction increases the cumulative infiltration and limits to the kinematic approximation as $C \to 0$. In general, Ψ, cannot be assumed to be constant but the more complex model by Selker et al. (1999) which assumes an exponential decay of Ψ with depth gives similar results. On the whole all three models give very similar results, but the additional fitting parameter in Green-Ampt type models can be chosen to improve the fit to the data.

6 Conclusion

In soils with declining porosity and hydraulic conductivity transitional infiltration leads to the formation of a saturated region at depth that limits the cumulative infiltration. This case has received little attention due to the complex interaction between unsaturated and saturated regions. A particular challenge is the dynamically changing shape of the saturated region. To study these flows we neglect capillary forces and extend the kinematic wave analysis for unsaturated flow to the saturated region. This is possible only in one-dimension where analytic expressions for the flux in the saturated region are available. The resulting extended kinematic wave approximation gives (semi-) analytic solutions and allows an analysis of coupled unsaturated-saturated flows.

We have applied this theory to transitional infiltration into soils with three different decaying soil porosity profiles: two-layer, exponential and power-law. In all cases, the infiltration process can be divided into three stages: I) Initially an unsaturated wetting front propagates into the soil and the rate of infiltration is constant. II) A saturated regions forms at depth and leads to the formation of a rising perched water table. Although the saturated region chokes the downward flow the infiltration rate into the soil remains constant. III) As the water table reaches the surface the infiltration rate drops instantaneously and leads to ponding of the rainfall and runoff. After ponding the saturated wetting front propagating into the soil slows down and the infiltration rate declines further. For the special case of a two-layer soil, we show that the flux in the saturated region does not depend on time so that all fronts speeds remain constant until ponding occurs (Stages I and II). This time invariant structure allows an analysis with the method of characteristics resulting in explicit analytic solutions that give insight into the propagation of saturations and the paths of fluid particles through the soil.

All solutions show excellent agreement with numerical solutions of the governing equations in the limit of no capillary forces. For the two-layer soil our analytic solutions compare well to numerical solutions of the full Richards equation with Hydrus 1D. Similarly, our solutions compare well with experimental data for infiltration into a multi-layer soil with declining hydraulic conductivity. In this case, capillary forces are not negligible, so that the kinematic solution underestimates the cumulative infiltration by approximately 6%.

The extended kinematic wave analysis introduced here is therefore an important tool to understand the behavior of Richards equation in the limit of negligible capillary forces. In particular it allows the analysis of the interaction between unsaturated and saturated regions within the soil. This approach can be extended to arbitrary one-dimensional soil profiles with more complex initial saturation distributions. The (semi-) analytical

nature of the solutions and the explicit prediction of the depth of the water table are advantageous for the integration into land surface models.

Acknowledgments

Support for this work was provided through NASA under Emerging World Grant number NASA 18−EW18_2−0027 and University of Texas Institute for Geophysics under Graduate Student Fellowship. The authors acknowledge the discussions with Cyril Grima and Anja Rutishauser that motivated this work.

Data Availability Statement

Python scripts that evaluate the (semi-) analytical solutions and generate all figures based on these solutions are available on Zenodo: https://zenodo.org/record/7080194 (Shadab & Hesse, 2022b). Hydrus 1D simulation files and the code for its analysis are also provided.

Appendix A Full two-phase flow formulation

The full system is composed of two phases, water and gas, in a non-deforming and stationary porous medium with porosity ϕ and permeability k. The transport equations for the water and gas phases can be respectively written as follows

$$\phi \frac{\partial}{\partial t}(\rho s) + \nabla \cdot (\rho \mathbf{q}) = 0 \tag{A1}$$

$$\phi \frac{\partial}{\partial t}(\rho_g s_g) + \nabla \cdot (\rho_g \mathbf{q}_g) = 0 \tag{A2}$$

where subscript g refers to the gas phase quantities. The corresponding water phase quantities have no subscripts for brevity. The saturation, density and volumetric flux of water [gas] phase are given by s [s_g], ρ [ρ_g] and $\mathbf{q}$ [$\mathbf{q}_g$], respectively. Equations (A1) and (A2) can be combined to yield the following two-phase continuity equation

$$\nabla \cdot (\mathbf{q} + \mathbf{q}_g) = 0. \tag{A3}$$

The volumetric flux in water and gas phases can be respectively written as an extension to Darcy's law,

$$\mathbf{q} = -\frac{\mathrm{k} k_{rw}}{\mu}(\nabla p - \rho \mathbf{g}) \quad \text{and} \quad \mathbf{q}_g = -\frac{\mathrm{k} k_{rg}}{\mu_g}(\nabla p_g - \rho_g \mathbf{g}) \tag{A4}$$

where $\mathbf{q}$ [$\mathbf{q}_g$] is the Darcy's volumetric flux of water [gas] phase ($\mathrm{m}^3/\mathrm{m}^2.\mathrm{s}$), k_{rw} [k_{rg}] is the relative permeability of water [gas] and μ [μ_g] is the dynamic viscosity of water [gas] (Pa.s). Relative permeabilites k_{rw} and k_{rg} are function of water saturation s (Wyckoff & Botset, 1936). The absolute permeability of the porous medium (m^2), given by k, is a function of the porosity ϕ. The pressures ($\mathrm{kg/m.s}^2$) for water and gas phases are p and p_g respectively. The acceleration due to gravity ($\mathrm{m/s}^2$) is given by $\mathbf{g} = g\hat{\mathbf{z}}$. The system of equations is closed by the constitutive relation for capillary pressure p_c

$$p_c(s) = p_g - p, \tag{A5}$$

which relates the two phase pressures and is typically assumed to be a function of saturation only (Leverett, 1941; Brooks & Corey, 1964; van Genuchten, 1980). The constitutive functions for multi-phase flow, k_{rw}, k_{rg} and p_c, display complex hysteresis (Blunt, 2017), but here we only consider the simplest case.

Appendix B Connection between full two phase flow equations and Richards equation

In order to derive Richards equation from the full two-phase flow equations we rewrite water saturation equation (A1) and total mass balance (A3) by substituting Darcy's law (A4),

$$\phi\frac{\partial s}{\partial t} - \nabla\cdot\left[\frac{\mathrm{k}k_{rw}}{\mu}\left(\nabla p - \rho\mathbf{g}\right)\right] = 0, \tag{B1}$$

$$\nabla\cdot\left[-\frac{\mathrm{k}k_{rw}}{\mu}(\nabla p - \rho\mathbf{g}) - \frac{\mathrm{k}k_{rg}}{\mu_g}(\nabla p_g - \rho_g\mathbf{g})\right] = 0. \tag{B2}$$

In one-dimensional depth coordinates, (B2) can be integrated as follows

$$-\frac{\mathrm{k}k_{rw}}{\mu}\left(\frac{\partial p}{\partial z} - \rho g\right) - \frac{\mathrm{k}k_{rg}}{\mu_g}\left(\frac{\partial p_g}{\partial z} - \rho_g g\right) = q_T, \tag{B3}$$

where q_T is the total flux across the domain. Moving terms to the right, we get

$$\frac{\mathrm{k}k_{rw}}{\mu}\left(\frac{\partial p}{\partial z} - \rho g\right) = -q_T - \frac{\mathrm{k}k_{rg}}{\mu_g}\left(\frac{\partial p_g}{\partial z} - \rho_g g\right). \tag{B4}$$

Substituting the capillary pressure p_c from Equation (A5) in (B4) gives

$$\frac{\mathrm{k}k_{rw}}{\mu}\left(\frac{\partial p}{\partial z} - \rho g\right) = -q_T - \frac{\mathrm{k}k_{rg}}{\mu_g}\left[\frac{\partial(p_c + p)}{\partial z} - (\rho_g - \rho + \rho)g\right], \tag{B5}$$

$$\frac{\mathrm{k}k_{rw}}{\mu}\left(\frac{\partial p}{\partial z} - \rho g\right) = -q_T - \frac{\mathrm{k}k_{rg}}{\mu_g}\left[\frac{\partial p_c}{\partial z} - (\rho_g - \rho)g\right] - \frac{\mathrm{k}k_{rg}}{\mu_g}\left(\frac{\partial p}{\partial z} - \rho g\right). \tag{B6}$$

Moving the last term on RHS to the left gives

$$\mathrm{k}\left(\frac{k_{rw}}{\mu} + \frac{k_{rg}}{\mu_g}\right)\left(\frac{\partial p}{\partial z} - \rho g\right) = -q_T - \frac{\mathrm{k}k_{rg}}{\mu_g}\left[\frac{\partial p_c}{\partial z} + \left(1 - \frac{\rho_g}{\rho}\right)\rho g\right]. \tag{B7}$$

Taking μ_g common from the denominator of LHS,

$$\mathrm{k}\frac{1}{\mu_g}\left(\frac{\mu_g}{\mu}k_{rw} + k_{rg}\right)\left(\frac{\partial p}{\partial z} - \rho g\right) = -q_T - \frac{\mathrm{k}k_{rg}}{\mu_g}\left[\frac{\partial p_c}{\partial z} + \left(1 - \frac{\rho_g}{\rho}\right)\rho g\right] \tag{B8}$$

Multiplying both sides by $\frac{\frac{\mu_g}{\mu}k_{rw}}{\frac{\mu_g}{\mu}k_{rw}+k_{rg}}$ gives

$$\mathrm{k}\frac{k_{rw}}{\mu}\left(\frac{\partial p}{\partial z} - \rho g\right) = -\frac{\frac{\mu_g}{\mu}k_{rw}}{\frac{\mu_g}{\mu}k_{rw} + k_{rg}}q_T - \frac{\mathrm{k}k_{rg}}{\mu_g}\frac{\frac{\mu_g}{\mu}k_{rw}}{\frac{\mu_g}{\mu}k_{rw} + k_{rg}}\left[\frac{\partial p_c}{\partial z} + \left(1 - \frac{\rho_g}{\rho}\right)\rho g\right] \tag{B9}$$

$$= -\frac{\mu_g}{\mu}\frac{k_{rw}}{\frac{\mu_g}{\mu}k_{rw} + k_{rg}}q_T - \frac{\mathrm{k}}{\mu}\frac{k_{rw}k_{rg}}{\frac{\mu_g}{\mu}k_{rw} + k_{rg}}\left[\frac{\mathrm{d}p_c}{\mathrm{d}s}\frac{\partial s}{\partial z} + \left(1 - \frac{\rho_g}{\rho}\right)\rho g\right] \tag{B10}$$

where chain rule has been used for $p_c(s)$. Finally, substituting (B10) into 1D version of (B1) gives

$$\phi\frac{\partial s}{\partial t} + \frac{\partial}{\partial z}\left(\mathcal{F}(s) - \mathcal{D}(s)\frac{\partial s}{\partial z}\right) = 0 \tag{B11}$$

where advective flux $\mathcal{F}(s)$ and diffusive flux $\mathcal{D}(s)$ components are given as

$$\mathcal{F}(s) = \frac{\mu_g}{\mu}\frac{k_{rw}}{\frac{\mu_g}{\mu}k_{rw} + k_{rg}}q_T + \frac{\mathrm{k}}{\mu}\frac{k_{rw}k_{rg}}{\frac{\mu_g}{\mu}k_{rw} + k_{rg}}\left(1 - \frac{\rho_g}{\rho}\right)\rho g, \tag{B12}$$

$$\mathcal{D}(s) = -\frac{\mathrm{k}}{\mu}\frac{k_{rw}k_{rg}}{\frac{\mu_g}{\mu}k_{rw} + k_{rg}}\frac{\mathrm{d}p_c}{\mathrm{d}s}. \tag{B13}$$

Now assuming that gas density and viscosity are much less compared to that of water, i.e., $\mu_g/\mu \ll 1$ and $\rho_g/\rho \ll 1$, as given in Kees (2004). This leads to a simplification in flux equations (B12 & B13) as

$$\mathcal{F}(s) = \frac{\mathrm{k}k_{rw}}{\mu}\rho g, \tag{B14}$$

$$\mathcal{D}(s) = -\frac{\mathrm{k}k_{rw}}{\mu}\frac{\mathrm{d}p_c}{\mathrm{d}s}. \tag{B15}$$

Therefore, the water saturation evolution equation (B11) becomes

$$\phi\frac{\partial s}{\partial t} + \frac{\partial}{\partial z}\left(\frac{\mathrm{k}k_{rw}}{\mu}\rho g + \frac{\mathrm{k}k_{rw}}{\mu}\frac{\mathrm{d}p_c}{\mathrm{d}s}\frac{\partial s}{\partial z}\right) = 0 \tag{B16}$$

Next introducing the variables,

$$\text{Soil moisture content / volume fraction of water, } \theta(s) := \frac{\text{Volume of water}}{\text{Total volume}} = \phi s, \tag{B17}$$

$$\text{Hydraulic conductivity } (m/s),\ K(\theta) := \frac{\mathrm{k}(\theta)k_{rw}(\theta)}{\mu}\rho g, \tag{B18}$$

$$\text{Capillary suction head } (m),\ \Psi(\theta) := p_c(\theta)/\rho g. \tag{B19}$$

Since porosity, ϕ, is invariant with time it can be combined with s to yield soil moisture content. Lastly, combining the capillary pressure terms transforms (B16) into final form of Richards equation (Richards, 1931) as

$$\frac{\partial\theta}{\partial t} + \frac{\partial}{\partial z}\left(K(\theta) + K(\theta)\frac{\partial\Psi(\theta)}{\partial z}\right) = 0. \tag{B20}$$

Although here we derive the Richards equation in soil moisture content (θ) form, we use its saturation (s) form in this manuscript.

References

Assouline, S. (2013). *Infiltration into soils: Conceptual approaches and solutions* (Vol. 49) (No. 4). Blackwell Publishing Ltd. doi: 10.1002/wrcr.20155

Beven, K. (1982). On subsurface stormflow: An analysis of response times. *Hydrological Sciences Journal*, *27*(4), 505–521. doi: 10.1080/02626668209491129

Beven, K. (1984). Infiltration into a class of vertically non-uniform soils. *Hydrological Sciences Journal*, *29*(4), 425–434. doi: 10.1080/02626668409490960

Blunt, M. (2017). *Multiphase Flow in Permeable Media.* Cambridge: Cambridge University Press. doi: 10.1017/9781316145098

Brooks, R., & Corey, T. (1964). Hydrau uc properties of porous media. *Hydrology Papers, Colorado State University*, *24*, 37.

Brutsaert, W., et al. (2005). *Hydrology: an introduction.* Cambridge University Press.

Carman, P. C. (1937). Fluid flow through granular beds. *Trans. Inst. Chem. Eng.*, *15*, 150–166.

Carsel, R. F., & Parrish, R. S. (1988). Developing joint probability distributions of soil water retention characteristics. *Water resources research*, *24*(5), 755–769.

Charbeneau, R. (1984). *Kinematic Models for Soil Moisture and Solute Transport* (Vol. 20; Tech. Rep. No. 6).

Cherry, J., & Freeze, A. (1979). *Groundwater* (1st ed.). Prentice Hall.

Childs, E. C., & Bybordi, M. (1969, 4). The vertical movement water in stratified porous material: 1. Infiltration. *Water Resources Research*, *5*(2), 446–459. doi: 10.1029/WR005i002p00446

Clapp, R., & Hornberger, G. (1978, 8). Empirical equations for some soil hydraulic properties. *Water Resources Research*, *14*(4), 601–604. Retrieved from http://doi.wiley.com/10.1029/WR014i004p00601 doi: 10.1029/WR014i004p00601

Clark, M., Fan, Y., Lawrence, D., Adam, J., Bolster, D., Gochis, D., ... Zeng, X. (2015, 8). Improving the representation of hydrologic processes in Earth System Models. *Water Resources Research*, *51*(8), 5929–5956. doi: 10.1002/2015WR017096

Clark, M., Nijssen, B., & Luce, C. (2017, 1). An analytical test case for snow models. *Water Resources Research*, *53*(1), 909–922. Retrieved from http://doi.wiley.com/10.1002/2016WR019672 doi: 10.1002/2016WR019672

Colbeck, S. C. (1972, 1). A Theory of Water Percolation in Snow. *Journal of Glaciology*, *11*(63), 369–385. Retrieved from https://www.cambridge.org/core/product/identifier/S0022143000022346/type/journal_article doi: 10.3189/S0022143000022346

Corradini, C., Melone, F., & Smith, R. (2000). Modeling local infiltration for a two-layered soil under complex rainfall patterns. *Journal of Hydrology*, *237*(1-2), 58–73.

Cueto-Felgueroso, L., & Juanes, R. (2008, 12). Nonlocal Interface Dynamics and Pattern Formation in Gravity-Driven Unsaturated Flow through Porous Media. *Physical Review Letters*, *101*(24), 244504. Retrieved from https://link.aps.org/doi/10.1103/PhysRevLett.101.244504 doi: 10.1103/PhysRevLett.101.244504

Dai, Y., Zhang, S., Yuan, H., & Wei, N. (2019, 10). Modeling Variably Saturated Flow in Stratified Soils With Explicit Tracking of Wetting Front and Water Table Locations. *Water Resources Research*, *55*(10), 7939–7963. Retrieved from https://onlinelibrary.wiley.com/doi/abs/10.1029/2019WR025368 doi: 10.1029/2019WR025368

DiCarlo, D. (2005). Modeling observed saturation overshoot with continuum additions to standard unsaturated theory. *Advances in Water Resources*, *28*(10 SPEC. ISS.), 1021–1027. doi: 10.1016/j.advwatres.2004.12.003

DiCarlo, D. (2013). Stability of gravity-driven multiphase flow in porous media: 40 Years of advancements. *Water Resources Research*, *49*(8), 4531–4544. doi: 10.1002/wrcr.20359

Dunne, T. (1978). Field studies of hillslope flow processes. In M. Kirkby (Ed.), *Hillslope hydrology* (pp. 227–293). Chichester, UK: John Wiley & Sons, Ltd.

Farthing, M. W., & Ogden, F. L. (2017). Numerical Solution of Richards Equation: A Review of Advances and Challenges. *Soil Science Society of America Journal*, *0*(0), 0. Retrieved from https://dl.sciencesocieties.org/publications/sssaj/abstracts/0/0/sssaj2017.02.0058 doi: 10.2136/sssaj2017.02.0058

Green, W., & Ampt, G. (1911). Studies on Soil Phyics. *The Journal of Agricultural Science*, *4*(1), 1–24. Retrieved from https://www.cambridge.org/core/product/identifier/S0021859600001441/type/journal_article doi: 10.1017/S0021859600001441

Hassanizadeh, S. M., & Gray, W. G. (1993, 10). Thermodynamic basis of capillary pressure in porous media. *Water Resources Research*, *29*(10), 3389–3405. Retrieved from http://doi.wiley.com/10.1029/93WR01495 doi: 10.1029/93WR01495

Horton, R. E. (1933). The role of infiltration in the hydrologic cycle. *Eos, Transactions American Geophysical Union*, *14*(1), 446–460.

Kale, R., & Sahoo, B. (2011). *Green-Ampt Infiltration Models for Varied Field Conditions: A Revisit* (Vol. 25) (No. 14). doi: 10.1007/s11269-011-9868-0

Kees, C. E. (2004). *Speed of propagation for some models of two-phase flow in porous media* (Tech. Rep.). North Carolina State University. Center for Re-

search in Scientific Computation.

Keller, T., & Or, D. (2022). Farm vehicles approaching weights of sauropods exceed safe mechanical limits for soil functioning. *Proceedings of the National Academy of Sciences*, *119*(21), e2117699119.

Kozeny, J. (1927). Uber kapillare leitung der wasser in boden. *Royal Academy of Science, Vienna, Proc. Class I*, *136*, 271–306.

LeVeque, R. (1992). *Numerical Methods for Conservation Laws*. Birkhaeuser Verlag.

Leverett, M. (1941). Capillary Behavior in Porous Solids. *Transactions of the AIME*, *142*(01), 152–169. Retrieved from `http://www.onepetro.org/doi/10.2118/941152-G` doi: 10.2118/941152-G

Mein, R., & Larson, C. (1973). Modeling infiltration during a steady rain. *Water Resources Research*, *9*(2), 384–394. Retrieved from `http://doi.wiley.com/10.1029/WR009i002p00384` doi: 10.1029/WR009i002p00384

Meyer, C., & Hewitt, I. (2017). A continuum model for meltwater flow through compacting snow. *Cryosphere*, *11*(6), 2799–2813. doi: 10.5194/tc-11-2799-2017

Milly, P. (1988). Advances in modeling of water in the unsaturated zone. *Transport in porous media*, *3*(5), 491–514.

Morbidelli, R., Corradini, C., Saltalippi, C., Flammini, A., Dari, J., & Govindaraju, R. (2018b). Rainfall infiltration modeling: A review. *Water*, *10*(12). doi: 10.3390/w10121873

Morbidelli, R., Corradini, C., Saltalippi, C., Flammini, A., Dari, J., & Govindaraju, R. S. (2018a). Rainfall infiltration modeling: A review. *Water*, *10*(12), 1873.

Nachabe, M. (1996). Macroscopic capillary length, sorptivity, and shape factor in modeling the infiltration rate. *Soil Science Society of America Journal*, *60*(4), 957–962.

Navas-Montilla, A., & Murillo, J. (2017). Overcoming numerical shockwave anomalies using energy balanced numerical schemes. application to the shallow water equations with discontinuous topography. *Journal of Computational Physics*, *340*, 575–616.

Nimmo, J. (2021). The processes of preferential flow in the unsaturated zone. *Soil Science Society of America Journal*, *85*(1), 1–27. doi: 10.1002/saj2.20143

Philip, J. (1957). The theory of infiltration. *Soil Science*, *83*(5), 345–358. doi: 10.1097/00010694-195705000-00002

Rhee, H.-K., Aris, R., & Amundson, N. (2001). *First-order partial differential equations, Volume 1: Theory and applications of single equations*. Dover Books on Mathematics.

Richards, L. A. (1931). Capillary conduction of liquids through porous mediums. *Physics*, *1*(5), 318–333.

Richardson, L. F. (1922). *Weather prediction by numerical process*. University Press.

Rupp, D. E., & Selker, J. S. (2005). Drainage of a horizontal boussinesq aquifer with a power law hydraulic conductivity profile. *Water Resources Research*, *41*(11).

Selker, J. S., Duan, J., & Parlange, J.-Y. (1999). Green and ampt infiltration into soils of variable pore size with depth. *Water resources research*, *35*(5), 1685–1688.

Shadab, M. A., & Hesse, M. (2022a). A hyperbolic-elliptic model and conservative numerical method for gravity-dominated variably-saturated groundwater flow. *arXiv preprint arXiv:2210.04724*. Retrieved from `http://arxiv.org/abs/2210.04724`

Shadab, M. A., & Hesse, M. A. (2022b, May). *mashadab/hyperbolic-infiltration-theory: v1.0.* Zenodo. Retrieved from `https://doi.org/10.5281/zenodo.7080194` doi: 10.5281/zenodo.7080194

Šimunek, J., Van Genuchten, M. T., & Šejna, M. (2012). Hydrus: Model use, calibration, and validation. *Transactions of the ASABE*, *55*(4), 1263–1274.

Singh, V., Bengtsson, L., & Westerstrom, G. (1997, 2). Kinematic wave mod-

elling of vertical movement of snowmelt water through a snowpack. *Hydrological Processes*, *11*(2), 149–167. Retrieved from http://doi.wiley.com/10.1002/%28SICI%291099-1085%28199702%2911%3A2%3C149%3A%3AAID-HYP427%3E3.3.CO%3B2-F doi: 10.1002/(SICI)1099-1085(199702)11:2⟨149::AID-HYP427⟩3.3.CO;2-F

Sisson, J., Ferguson, A., & van Genuchten, M. (1980, 11). Simple Method for Predicting Drainage from Field Plots. *Soil Science Society of America Journal*, *44*(6), 1147–1152. Retrieved from http://doi.wiley.com/10.2136/sssaj1980.03615995004400060004x doi: 10.2136/sssaj1980.03615995004400060004x

Smith, R. (1983, 1). Approximate Soil Water Movement by Kinematic Characteristics. *Soil Science Society of America Journal*, *47*(1), 3–8. Retrieved from http://doi.wiley.com/10.2136/sssaj1983.03615995004700010001x doi: 10.2136/sssaj1983.03615995004700010001x

Te Chow, V. (2010). *Applied hydrology*. Tata McGraw-Hill Education.

van Genuchten, M. (1980). A Closed-form Equation for Predicting the Hydraulic Conductivity of Unsaturated Soils1. *Soil Science Society of America Journal*, *44*(5), 892. doi: 10.2136/sssaj1980.03615995004400050002x

Vereecken, H., Weihermüller, L., Assouline, S., Šimnek, J., Verhoef, A., Herbst, M., ... Xue, Y. (2019, 1). Infiltration from the Pedon to Global Grid Scales: An Overview and Outlook for Land Surface Modeling. *Vadose Zone Journal*, *18*(1), 1–53. Retrieved from https://onlinelibrary.wiley.com/doi/10.2136/vzj2018.10.0191 doi: 10.2136/vzj2018.10.0191

Vogel, T., & Cislerova, M. (1988, 2). On the reliability of unsaturated hydraulic conductivity calculated from the moisture retention curve. *Transport in Porous Media*, *3*(1), 1–15. Retrieved from http://link.springer.com/10.1007/BF00222683 doi: 10.1007/BF00222683

Wyckoff, R. D., & Botset, H. G. (1936). The flow of gas-liquid mixtures through unconsolidated sands. *Journal of Applied Physics*, *7*(921), 325–345. doi: 10.1063/1.1745402

Zha, Y., Yang, J., Zeng, J., Tso, C.-H. M., Zeng, W., & Shi, L. (2019). Review of numerical solution of richardson–richards equation for variably saturated flow in soils. *Wiley Interdisciplinary Reviews: Water*, *6*(5), e1364.